OCS Study
BOEM 2022-079

Central Beaufort Sea Wave and Hydrodynamic Modeling Study

Report 2: Modeled waves, hydrodynamics, and sediment transport within Foggy Island Bay

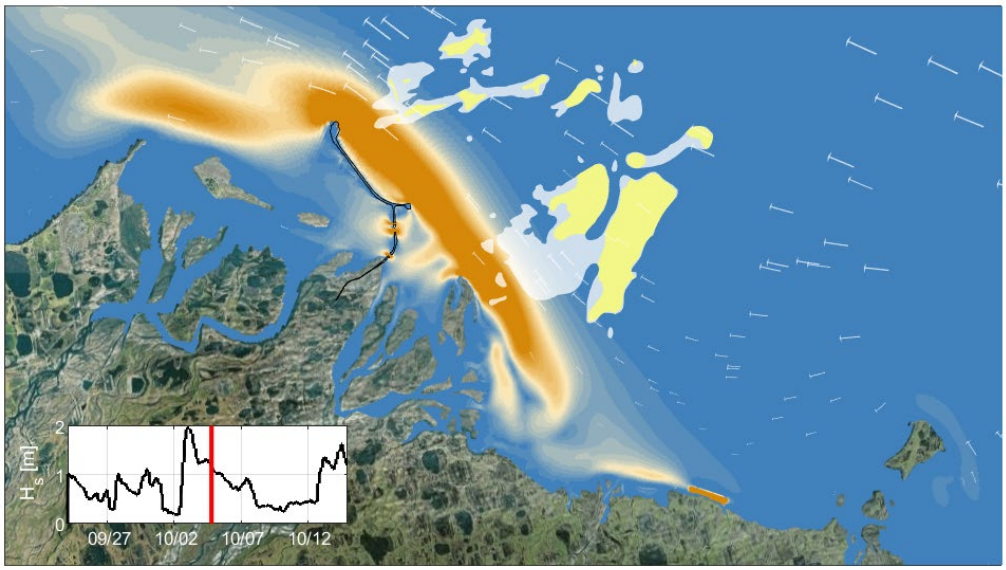

U.S. Department of the Interior
Bureau of Ocean Energy Management
Ocean Energy Management, Anchorage, AK

BOEM
Bureau of Ocean Energy Management

OCS Study
BOEM 2022-079

Central Beaufort Sea Wave and Hydrodynamic Modeling Study

Report 2: Modeled waves, hydrodynamics, and sediment transport within Foggy Island Bay

March 2023

Authors:
Li H. Erikson
Kees Nederhoff
Anita Engelstad
Jeremy Kasper
Peter Bieniek

Prepared under Interagency Agreement M17PG00046
by
U.S. Geological Survey
Pacific Coastal and Marine Science Center
2885 Mission Street
Santa Cruz, CA 95060

And under Cooperative Agreement M17AC00020
by
Alaska Center for Energy and Power
University of Alaska Fairbanks
1764 Tanana Loop
Fairbanks, AK 99775

U.S. Department of the Interior
Bureau of Ocean Energy Management
Ocean Energy Management, Anchorage, AK

BOEM
Bureau of Ocean Energy Management

DISCLAIMER

Study collaboration and funding were provided by the U.S. Department of the Interior, Bureau of Ocean Energy Management (BOEM), Environmental Studies Program, Washington, DC, under Agreement Number M17AC00020 with University of Alaska and through Intra-Agency Agreement Number M17PG00046 with the U.S. Geological Survey Pacific Coastal and Marine Science Center.

This report has been technically reviewed by BOEM, and it has been approved for publication. This report has been peer reviewed and approved for publication consistent with USGS Fundamental Science Practices (https://pubs.usgs.gov/circ/1367/). The views and conclusions contained in this document are those of the authors and should not be interpreted as representing the opinions or policies of BOEM. Any use of trade, firm, or product names is for descriptive purposes only and does not imply endorsement or recommendation by the U.S. Government.

CITATION

Erikson, L.H, Nederhoff, L., Engelstad, A., Kasper, J., Bieniek, P., U.S. Geological Survey (USGS, Pacific Coastal Marine Science Center, Santa Cruz, CA). 2022. Central Beaufort Sea wave and hydrodynamic modeling study. Report 2: Modeled waves, hydrodynamics and sediment transport in Foggy Island Bay. Anchorage (AK): U.S. Department of the Interior, Bureau of Ocean Energy Management.40 p. plus appendices. Report No.: OCS Study BOEM 2022-079. IAA No.: M17PG00046.

ABOUT THE COVER

Snapshot of a model simulation showing transport of hypothetical fine-grained sediment placed on the beach following mass wasting of the bluff. The figure and further details can be found in Report 1 of this 2-part report series.

ACKNOWLEDGMENTS

We thank Heather Crowley, Thomas Kilpatrick, and Caryn Smith at BOEM and Thomas Lorenson at USGS for their thoughtful reviews. We thank Stuart Pearson at Deltares for the development of and guidance and help with SedTRAILS to visualize the modeled sediment transport potentials.

Contents

List of Figures ..... **iii**

List of Tables ..... **iv**

List of Abbreviations and Acronyms ..... **v**

1 Introduction **6**

2 Data and methods **7**

2.1 Boundary conditions 7

2.1.1 Hindcast model runs: 1979 through 2019 7

2.1.2 Projection model runs: 2020 through 2050 8

2.2 Simulation methods 9

2.2.1 Time-series wave statistics 10

2.2.2 Sediment transport potentials 12

3 Results **14**

3.1 Water levels 14

3.2 Waves 15

3.2.1 Temporal changes 16

3.2.2 Local comparison of wave variables 19

3.2.3 Projected changes in return period wave heights 23

3.3 Sediment-transport potentials (vector fields) 24

3.3.1 Sea states 24

3.3.2 Hindcast model runs (ERA5) 30

3.3.3 Projected sediment transport potentials 33

3.3.4 Transport of a fluvial sediment plume 36

4 Conclusions and future directions **38**

5 References **41**

Appendix A: List of available data files produced for this study **46**

Appendix B: Supplementary figures **63**

List of Figures

Figure 2.1 Flow chart showing an overview of the modeling approaches for achieving continuous wave time-series and multi-decadal scale mean sediment transport fields within Foggy Island Bay. 10

Figure 2.2 Maps showing Model Tier 2B and point location where Tier 1 data were extracted 11

Figure 2.3 Flow chart showing the steps used to generate representative sea states for simulation of sediment transport potentials over multi-decadal timescales..... 13

Figure 3.2 Difference in mean, 95th, and 99.5th percentile wave heights between the hindcast and projected period. 16

Figure 3.3 Difference in probability of occurrence between projected and hindcasted winds..... 17

Figure 3.4 Open water days at Foggy Island Bay from 1979 through 2050. 18

Figure 3.5 Monthly local trends (70.27458, -147.5863) for mean and maximum wave heights. ... 19

Figure 3.6. Monthly annual local (70.27458, -147.5863) maximum wave heights from 1979 through 2050. 20

Figure 3.7. Changes in wave heights and corresponding sea ice cover from 1979 through 2049.22

Figure 3.9. Maps showing the hindcast and projected annual, 5 year, 10 year, and 20 year return period height return periods. 24

Figure 3.10. Snapshotos of two example sea states. 27

Figure 3.11 Sediment transport potential as visualized with SedTRAILS for the 30 different sea states identified. 28

Figure 3.12 Mean transport potentials per sediment class for the hindcast period, without LDI. .. 31

Figure 3.13 Mean sediment transport potential as visualized with SedTRAILS for model simulations without (red) and with the LDI in place (blue). 32

Figure 3.14 Analysis of net sediment erosion and deposition with and without the LDI in place for the hindcast period..... 36

Figure 3.15 Mean sediment transport potential as visualized with SedTRAILS for the hindcast and projection time-periods, including contributions from the individual downscaled climate models. 34

Figure 3.16 Maps showing the percent change in mean transport potentials projected with each GCM compared to the hindcast time-period. 35

Figure 3.17 Maximum transport of an assumed cohesive fluvial discharge plume under sea ice and without sea ice cover. 37

Figure A.1. Monthly annual local (70.27458, -147.5863) maximum wave periods from 1979 through 2050. 63

List of Tables

Table 2.1 Source products of projected wind, atmospheric pressures, and sea ice used as boundary conditions to compute stormtide and waves within Stefansson Sound 3

Table 3.1 Monthly trends in Tm and the LDI and offshore model boundary for the hindcast and projection time-periods. 15

Table 3.2 Overview of 30 representative sea states used within this study 20

Table 3.3 Occurrence probabilities of each sea state and model..... 23

List of Abbreviations and Acronyms

D_m	incident mean wave direction
H_s	significant wave height
T_m	mean wave period
m_o, m_1	0^{th} and 1^{st} moment of the wave spectrum
z_s	non-tidal water level variations (surge)
BOEM	Bureau of Ocean Energy Management
cm	centimeter(s)
CMIP	Coupled Model Intercomparison Project
CNRM	Centre National de Recherches Meteorologiques
DPP	Development and Production Plan
DWDB	downscaled wave database
ECEarth	European Consortium Earth Systems Model
ECMWF	European Centre for Medium-Range Weather Forecasts
ecWAM	European Consortium Weather Forecasting Ocean Wave Mmodel
ERA5	Fifth generation ECMWF atmospheric reanalysis
FIB	Foggy Island Bay
GCM	Global Climate Model or General Circulation Model
GFDL	Geophysical Fluid Dynamics Laboratory
GMT	Greenwich mean time
HadGemSST	Hadley Centre Global Environmental Model (United Kingdom)
kg	kilogram(s)
km	kilometer(s)
LDI	Liberty Development Island
m	meter(s)
MAE	mean absolute error
MDA	maximum dissimilarity method
P	wave power
RCP8.5	Representative Concentration Pathway 8.5 (climate scenario)
RMSE	root-mean-square error
s	seconds
SCI	scatter index
SedTrails	sediment transport visualization and Lagrangian simulator
SWAN	Simulating Waves Nearshore (wave model)
TSS	total suspended solids
U	wind speed
UAA	University of Alaska Anchorage
UAF	University of Alaska Fairbanks
Udir	wind direction
USGS	United States Geological Survey
WRF	Weather Research Forecasting model

1 Introduction

Renewed interest in nearshore oil exploration and production in the shallow waters of the Central Beaufort Sea Shelf has created a need to advance our understanding of the past, current, and future atmospheric and oceanographic conditions that affect existing and planned infrastructure and nearshore ecosystems. At the time of writing this report, Hilcorp Alaska, LLC, has received BOEM approval for an oil and gas Development and Production Plan (DPP) that includes the construction of the Liberty Drilling Island (LDI) in Foggy Island Bay, situated within Stefansson Sound circa 30 km east of Prudhoe Bay (Figure 1.1). The aim of this study is to investigate how longer periods of open water (defined as < 15% ice cover), decreased sea ice cover, and changes in ocean and atmospheric conditions might affect wave and storm surge conditions, sediment transport patterns, and coastal erosion rates within Foggy Island Bay as well as the modeled influence of the offshore artificial island on sediment transport patterns.

With the anticipated construction of the LDI, which is to be located near the southeast boundary of the Boulder Patch habitat (Figure 1.1c and 2.2), Coastal Frontiers (2014) used historical wind speeds and a combination of probabilistic, empirical, and analytical models to compute sediment transport pathways and possible impacts to the Boulder Patch during construction. The Boulder Patch is an ecologically important marine area believed to support the Beaufort Sea's richest and most diverse biological communities (Dunton and Schonberg 2000). Whilst Coastal Frontiers' findings show that construction activities are likely to produce suspended sediment plumes that will advect into the Boulder Patch area, the modeled influence of the LDI on sediment transport pathways during the design-life of the project is uncertain.

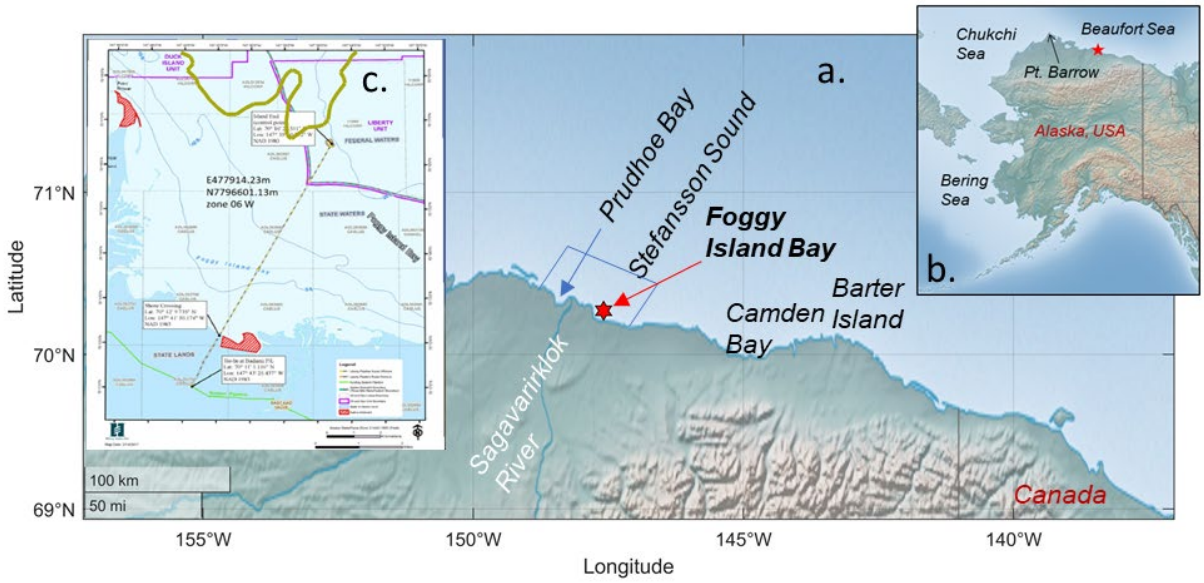

Figure 1.1 Map of study location.
Maps showing the greater region of Stefansson Sound and Foggy Island Bay (a,b). Red star denotes the location of the planned Liberty Drilling Island (LDI). (c) Chart of Foggy Island Bay and planned location as presented by Hilcorp Alaska, LLC, in a 2017 amendment to the construction plan (Hilcorp Alaska, LLC, 2017). The southern boundary of the Boulder Patch area, added to inset (c), is denoted with the thick yellow line.

This report, Report 2 of a 2-part series, describes results and findings of model production runs that were done to compute summary wave statistics and sediment transport patterns within Foggy Island Bay for the entirety of the hindcast (1979 – 2019) and projection time periods (2020 – 2050). The overall modeling scheme, including downscaling from the global to local scale as well as calibrations and validations of individual models, are provided in Report 1 (Kasper et al. 2023). In Section 2 of this document, we

summarize the governing datasets used to compute hindcasted and projected waves, hydrodynamics, and sediment transport. That section also describes application of the wave-hydrodynamic-sediment transport model, referred to as Tier 2C in Report 1 (Kasper et al. 2023), for decadal-scale simulations. In the results section (Section 3), we first compare past (1979 – 2019) extreme non-tidal water levels and wave conditions to projected (2020–2050) conditions, assuming the unmitigated climate scenario RCP8.5 (Riahi et al. 2011). We then present modeled sediment transport vectors and the potential for differences in sediment advection pathways into the Boulder Patch area with and without placement of the LDI. This report concludes with a summary of findings and discussion of perspectives for future research.

2 Data and methods

2.1 Boundary conditions

Governing datasets used to downscale and generate time series of hindcasted and projected waves, extreme water level variations, and sediment transport pathways are summarized in this section. These datasets are also presented in Report 1 (Kasper et al. 2022), where a few additional datasets were considered but excluded from further analyses (see Section 3.3.2 of Report 1).

2.1.1 Hindcast model runs: 1979 through 2019

The 5th generation ECMWF (European Centre for Medium-Range Weather Forecasts) atmospheric reanalysis (ERA5) products that date back to 1979 became available about mid-way through this study in January 2019 and have since emerged as prime products for accurately representing past climate and wave conditions across the globe (Molina et al. 2021; Erikson et al. 2022). The data cover the Earth on a 30 km grid and resolve the atmosphere using 137 levels from the surface up to a height of 80 km. ERA5 combines model data with vast amounts of past re-processed observations from across the world into a globally complete and consistent dataset (Hersbach et al. 2020). ERA5 was developed and is continuously produced by the European Centre for Medium-Range Weather Forecasts (ECMWF); it provides hourly estimates of several atmospheric, land and oceanic climate variables, and daily estimates of sea ice (https://cds.climate.copernicus.eu/cdsapp#!/home).

Relevant to this study are winds, atmospheric pressures, sea ice cover, and ocean waves. The atmospheric parameters are primarily derived from satellite radiances and scatterometers. The evolution of sea ice cover is derived from a number of products: it includes reprocessed data from the UK Met Office Hadley Centre, EUMETSAT, and the United Kingdom Meteorological Office (Hirahara et al. 2016). The wave data are derived from a fully coupled atmosphere-ocean-wave model (ecWAM), which assimilates satellite radar altimeter-derived wave height data from 1991-present. The ecWAM wave model is based on wind-wave growth parameterizations of WAM cycle 4 (commonly known as ST3).

As part of this study, we compared ERA5 winds to station observations (Bieniek et al. 2022) and ERA5 waves to buoy observations and our own wave computations using a variety of wind products (Kasper et al. 2022, Report 1, Section 3.5.2). We found that ERA5 showed good skill for both parameters. Considering the good skill, consistency of parameters, and continuous updating of this product (the time series is continuously updated and made available with a 3-month lag), it was decided that the use of ERA5 reanalysis products would serve as an efficient and coherent boundary condition for the Foggy Island Bay wave and sediment transport models.

2.1.2 Projection model runs: 2020 through 2050

When considering the influence of climate change, global climate models (GCMs) are the best tools available to drive oceanographic and coastal models for assessing future conditions and hazards. Even in regions where climatologies are well defined, wave conditions over the past several decades may not be indicative of the future wave climate since waves are the result of winds which are affected by climate change. Winds are driven by atmospheric variability and the complex interaction between the Earth's atmosphere and ocean systems, making it difficult to project future wind and consequent wave conditions. Whereas GCMs are routinely used for assessing climatological parameters, including changes in storm patterns, atmospheric variability, temperatures, and precipitation (Cayan et al. 2008; Chang et al. 2013; Sillman et al. 2013a,b; Barnes et al. 2014), these models generally do not provide parameterizations of ocean wind waves (Morim et al. 2020), necessitating the need to run large-scale (global to regional) wave models to generate time-series wave parameter metrics.

Because of the necessary geographic scale and multitude of parameters simulated that result in high computation costs, GCMs are typically run and provide coarse outputs on the order of 100 km or more. That scale is arguably sufficient for global scale wave models but is insufficient in estimating coastal processes across the continental shelf and to the nearshore. To this end, the 5th Coupled Model Intercomparison Project (CMIP5) Geophysical Fluid Dynamics Laboratory (GFDL) model was dynamically downscaled (Bieniek et al. 2016) to a 20 km resolution across Alaska. Winds and atmospheric pressures from this finer resolution GCM product were used as boundary conditions to the Tier 1 hydrodynamic and wave models to generate stormtide and wave time series offshore of Foggy Island Bay (see Report 1).

During the course of this study, a new set of GCM products became available through the 6th generation Coupled Model Intercomparison Project (CMIP6) (Eyring et al. 2016), for which several groups ran their GCMs on 25 to 50 km resolution grids to improve cloud vapor mix and cyclogenesis representations. The availability of these higher resolution GCM products allowed us to complement the use of the CMIP5-GFDL with three additional GCM products. The use of a multi-model average, or ensemble, is preferred for projecting future conditions because of large uncertainties in climate forcings, internal model variability, and storm geography (Wang and Swail 2005). The four spatiotemporally varying GCMs used to simulate stormtides and waves for years 2020 – 2050 in Stefansson Sound are listed in Table 2.1.

Table 2.1 Source products of projected wind, atmospheric pressures, and sea ice cover used as boundary conditions to compute stormtide and waves within Stefansson Sound

Global Climate Model	Spatial and temporal wind resolution	Spatial and temporal sea ice resolution	Model variant
CNRM	100 km / 3 hourly	25 km / daily	CNRM-CM6-1-HR-r1i1p1f2
EC-Earth	50 km / 3 hourly	25 km / daily	EC-Earth3P-HR-r1i1p1f1_gr (wind) EC-Earth3P-HR-r1i1p2f1_gr (ice)
WRF-GFDL-CM3	20 km / hourly	20 km / daily*	WRF dynamic downscale
HadGEM-SST	50 km / 3 hourly	25 km / daily	HadGEM3-GC31-HM_highresSST-future_r1i1p1f1_gn

*interpolated from original GFDL-CM3 native resolution (200 km / daily)

2.2 Simulation methods

The long time period and high spatial resolution required for this study necessitated the use of a nested modeling scheme and schematized wave climatologies to reduce computational expense. Global and regional scale wave and hydrodynamic models (Tier 1), driven by spatio-temporally varying wind, atmospheric pressure, and sea ice fields, were used to generate continuous time series along the open boundaries of local (Tier 2) models (Figure 2.1). Report 1 presents details of the model train and individual model calibrations and validations, and therefore are not repeated here.

At the project level, the calibrated and validated standalone Tier 2B wave model (Section 3.2.2, Report 1) was used to compute 3-hourly time series of waves, at a 200 m grid resolution, for the 40-year hindcast period and four separate 30-year projections (using forcings listed in Table 2.1); this results in an equivalent of hourly data over 40 + (4*30) = 160 years. An overview of the model application and equations used to compute time-series wave statistics are provided in Section 2.2.1 below.

A second nested model, Tier 2C, was used to simulate mobilization and transport of sediment by both wave and non-wave driven currents (Section 3.2.3, Report 1). The model was run with and without the LDI in place. The LDI was represented in the hydrodynamic-sediment transport grid (FLOW module) with so-called 'thin dams' and by 'obstacles' in the wave grid. Thin dams are defined at the velocity grid points and prohibit flow exchange between two adjacent computation cells whilst conserving water volume. The LDI 'obstacle' in the wave grid was defined by corner points of a polyline. The polyline obstacles partially or wholly interrupt the propagation of waves from one grid point to the next. The dam option was selected with transmission coefficients $\alpha = 2.6$ and $\beta = 0.15$ (Goda et al. 1967) for modulating incident wave conditions at the obstacle, no reflection, and a height of 4.6 m above mean sea level. LDI size, shape, and orientation were guided by scale drawings in the 2017 Hilcorp Alaska, LLC, development and production plan, Amendment 3. The seabed footprint is expected to be 9.71 hectares, which equates to three and four cells in the wave and hydrodynamic/sediment transport grids, respectively. Because annual averages of sediment transport pathways within Foggy Island Bay require computationally heavy simulations of coupled wave and hydrodynamic processes across high-resolution model grids (50 to 200 m) that cover nearly 3,000 km^2, it is computationally unfeasible to continuously model all the hindcast and projection scenarios that together equate to ~160 years. Therefore, input-reduction techniques that characterize the full range of wave, flow, and wind forcing conditions were used to make such simulations feasible (e.g., de Vriend et al. 1993; Lesser 2009; Stevens et al. 2020). The method employed for determining representative sea states is presented in Section 2.2.2 below.

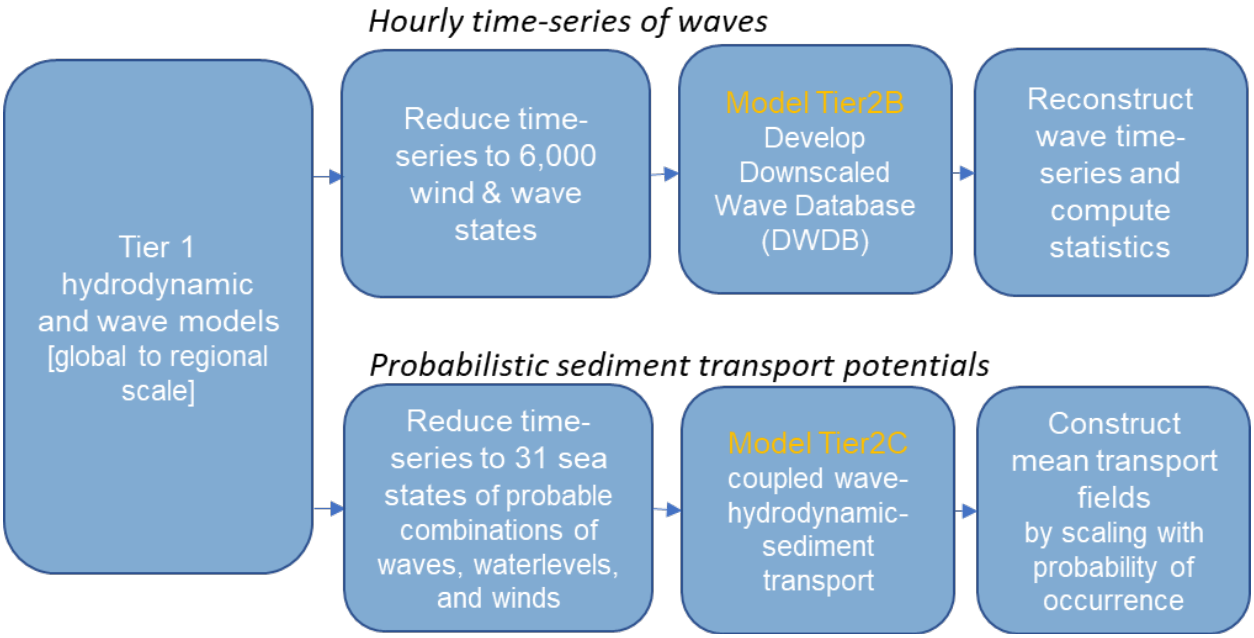

Figure 2.1 Flow chart showing an overview of the modeling approaches for achieving continuous wave time-series and multi-decadal scale mean sediment transport fields within Foggy Island Bay.

2.2.1 Time-series wave statistics

Wave summary statistics were computed from 3-hourly time series of wave fields reconstructed from a Downscaled Wave DataBase (DWDB). The DWDB was developed by running the calibrated and validated Tier 2B wave model (SWAN ver. 40.1ABCDE; Booij et al. 1999; Nederhoff et al. 2022; Engelstad et al., USGS Open-File-Report and Data Release, in press) for a set of 6,000 sea states (2,000 sea states for the hindcast period and 4,000 sea states for the projections). The sea-states represent distinct combinations of five parameters pulled from the Tier 1 hourly hindcast and projection time series (Figure 2.2): wave heights (H_s), mean wave periods (T_m), mean wave directions (D_m), wind speeds (U), and wind directions (U_{dir}). Sea states were identified using a multivariant maximum-dissimilarity algorithm (MDA). The MDA method bins all the data with particular care to include extreme events, allowing for a full representation of the marine climate (Camus et al. 2014). Continuous 3-hourly gridded wave field time series were then reconstructed by querying the DWDB with consecutive time-point data from each Tier1 simulation (hindcast and four projections as listed in Table 2.1). Further details on the reconstruction of time-series wave fields are provided in Report 1, Section 3.2.2, and Engelstad et al. USGS report (in press).

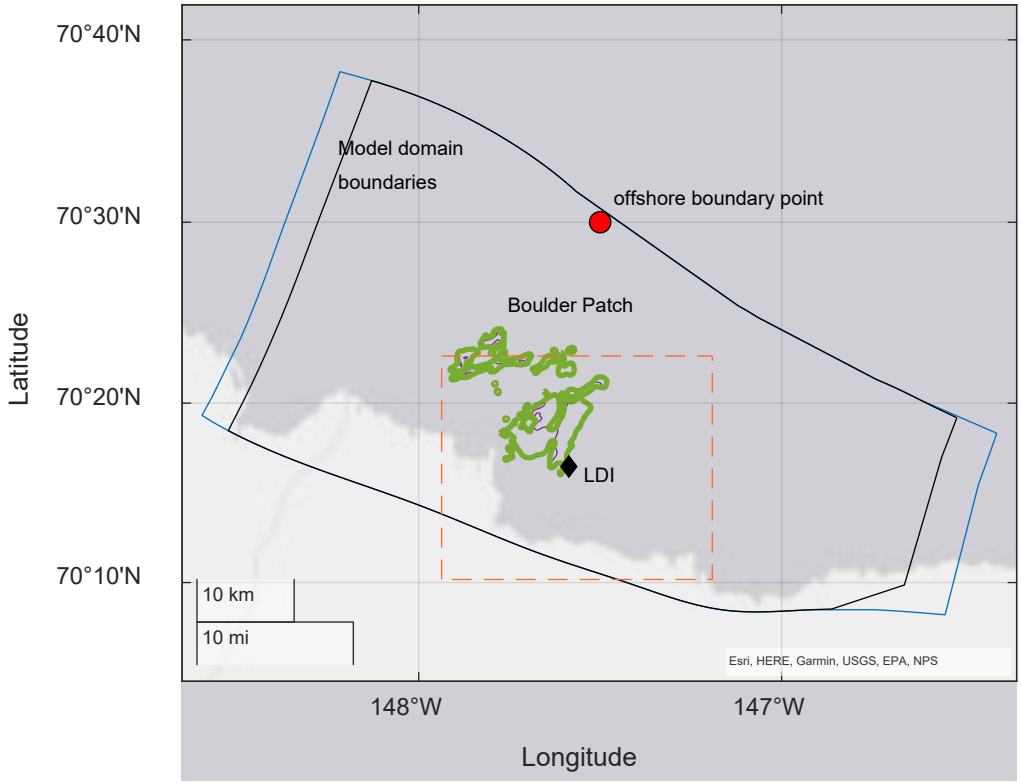

Figure 2.2 Map showing local level model boundaries, location of the primary offshore boundary point (red circle) and the planned Liberty Development Island (LDI) near the southeast region of the Boulder Patch (solid green and brown lines).
Blue and black solid lines denote the wave and hydrodynamic model boundaries, respectively. The dashed rectangle denotes the area of interest shown in Figures 3.2, 3.10, and 3.12.

Several summary statistics were computed from each of the continuous gridded time series:

Mean, max, and 25th, 50th, 75th, 90th, 95th, and 99.5th percentiles of H_s (m), T_m (s), D_m (degrees), steepness (H_s/L, dimensionless), near-bed orbital velocities (m/s), and wave power (P, Joules/m•s), where

$$H_s = 4\sqrt{m_0} \quad (1)$$

$$T_m = m_0/m_1 \quad (2)$$

$$L = gT_m{}^2/2\pi \quad (3)$$

$$P = EC_g \quad (4)$$

where E is the mean energy density per unit area of waves

$$E = \frac{1}{16}\rho g H_s^2 \quad (5)$$

and C_g is the group velocity (m/s) calculated iteratively with the dispersion relation for waves, which is dependent on local depth and wavelength (L, units of meters), and m_0 is the zero moment of the spectrum

and m_1 is the first moment of the spectrum; ρ is the density of water (1,028 kg/m^3), and g is the gravitational constant (9.83 m/s^2).

Additionally, H_s probabilities of exceedance statistics were computed for the annual, 2-yr, 5-yr, 10-yr, 20-yr, and 30-yr return periods. Because each time series is at least 30 years in length, exceedance statistics were computed by ranking the events and eliminating the need to fit a line through an assumed distribution (e.g., Generalized Extreme Value, GEV).

2.2.2 Sediment transport potentials

The Delft3D4 Modeling Suite (Lesser et al. 2004) was used to compute water motion, waves, and sediment transport within Foggy Island Bay. The hydrodynamic (Delft3D-FLOW) and wave module (Delft3D-WAVE (an implementation of SWAN in the Delft3D4 Modeling Suite)) were two-way coupled ('online mode'), enabling communication between the two modules so that depth variations and currents simulated with the hydrodynamics are implemented in the waves and vice-versa. Sediment transport was modeled with the online morphology module. Both cohesive and non-cohesive sediment were simulated. The sediment bed level was held constant in all simulations to reduce computation time, to decrease the uncertainty of morphodynamic updating, and to isolate the role of changing flows on the sediment-transport patterns that result from interactions with observed (known) morphologic features. Therefore, we speak of 'sediment transport potentials' throughout this study. For more information on the model setup, one is referred to Report 1 Section 3.2.3.

The model was implemented in two ways: as 1) continuous time series and 2) constructions from event-based simulations and probability of occurrence of those sea states. The continuous mode of implementation was done by applying coherent time series of Tier 1 waves, stormtides, and winds over relatively short timeframes (1–2 months). The results from those simulations provide temporally cohesive and continuous estimates of wave heights, currents, and sediment transport fields. Varying the sea ice cover and introducing hypothetical point-source sediment inputs from the Sagavanirktok River allowed for evaluation of dominant processes and the influence of sea ice on transport of sediment plumes.

To evaluate mean transports over multi-decadal timescales and for multiple GCM realizations (equating to ~160 years), and additionally the influence of the LDI on those transports, it was necessary to employ a data input reduction technique. With this method, sea states that characterize the full range of wave, stormtide, and wind forcing conditions were first identified. The coupled model (Tier 2C) was then run with forcing from each of the sea states. Lastly, the individual results were combined using the probability of occurrence per sea state over the time period of interest (40 years for the hindcast and 30 years for the projection).

Various data input reduction methods have been developed to identify representative sea states (de Vriend 1993; Camus 2014; Walstra et al. 2013; de Queiroz 2017). Here we employed the 'Input Reduction Tool' by Scheel (2017) and set the number of sea states to be 30 events plus an additional sea state of quiescent conditions that represent times of insignificant wave energy from the perspective of sediment mobilization due to either near-full ice cover (>85%) or small waves ($H_s < 0.5\ m$). The choice of 30 events is based on earlier work by Lesser (2009) and Hansen and Elias (2013), who considered 19 and 24 sea states, respectively, to be sufficient in representing sediment transport patterns and morphodynamic change along the high-energy U.S. west coast.

The full set of sea states, including H_s, T_m, D_m, surge (z_s), U, and U_{dir} was determined by clustering time-point data of H_s, T_m, and D_m from the ERA5 hindcast and GCM Tier 1 projections, and computing the mean of all water level variations (η), U, and U_{dir} that fall within each bin and meet the requirement of predominant setup (z_s > 5 cm) or setdown (z_s < 5 cm) conditions (Figure 2.3). Data points with $H_s <$ 0.5 m (considered quiescent), or with $110° < D_m < 290°$ and wind speeds < 12 m/s, were removed prior

to clustering. The latter test was implemented to reduce the number of time-points when modeled waves emanated from land. An exception was made for conditions when wind speeds exceeded 12 m/s; a condition that can cause rapid wave growth over relatively short fetch.

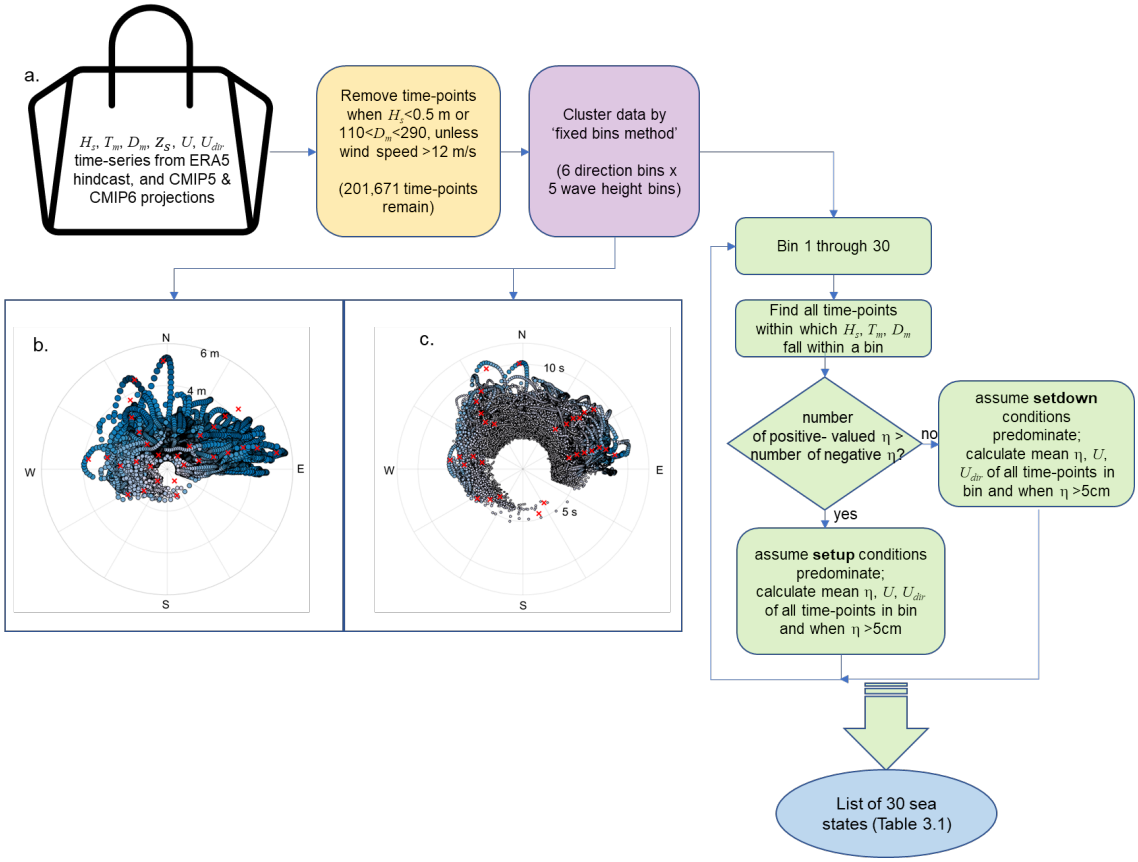

Figure 2.3 Flow chart showing the steps used to generate representative sea states for simulation of sediment transport potentials over multi-decadal timescales.
The flow chart is shown in (a.). Clustered combinations of H_s, T_m, and D_m, representing more than 200,000 individual time-points from the Tier 1 hindcast and projection wave model runs, are shown in (b.) and (c.) where the radial axis denotes wave heights (H_s) and wave periods (T_m), respectively. Individual time-points are shown with blue circles (sized according to H_s or T_m). Red 'x' denotes identified sea states.

3 Results

3.1 Storm surge and extreme sea water levels

Projected storm surge levels exhibit similar characteristics as noted for the hindcast period described in Report 1. Open water season storm surge events reached a maximum of 65 cm (excluding astronomic tides) seaward of Foggy Island Bay during the 41-year hindcast from 1979 through 2019. Note that depending on the co-occurrence of tides, these values can be up to 30 cm higher (as is the case for the maximum modeled stormtide, which was modeled to be 92 cm above MSL). These summary statistics are computed from 10-minute time-series outputs of the Tier 1 model at the 20 m isobath seaward of Foggy Island Bay. Variations in water levels produced with the finer resolution Tier 2 model are generally within 10% (higher and lower during setup and setdown events) at the LDI (~6 m water depth) compared to the offshore 20 m isobath location. Note also that very nearshore shallow regions (< 2 to 3 m water depth, MSL) can experience up to ~40% higher water levels in the Tier 2C model due to the ability of the finer mesh to resolve geomorphic features and flow hydrodynamics.

A small (-0.2 cm/year) but statistically significant ($pVal < 0.05$) negative trend of the 3-year moving mean annual maximum storm surge was found for the hindcast (Report 1, Figure 3.22). Extending the time series with the projected model ensemble mean of annual maximum surge levels indicates a continued weak negative trend but at an overall smaller rate of -0.1 cm/yr ($R^2 = 0.18$). A weak but statistically significant positive trend in the annual minimum surge levels (setdown) is also apparent (+0.1 cm/yr; $R^2 = 0.12$).

The annual maxima and minima surge levels exhibit decadal and semi-decadal oscillations, respectively (Figure 3.1). In Report 1, we compared the oscillations to established climate indices. Whereas no clear quantitative dependency between surge and climate indices were found, a qualitative correspondence between elevated storm surge levels with the negative phase of the Pacific Decadal Oscillation (PDO) was noted (Mantua et al. 1997). Qualitatively, it can be seen that the decadal signal continues throughout the projection period (red circles and triangles in Figure 3.1a). The signal is somewhat muted with the model ensemble (red circles) and is more apparent when considering the maximum levels within the model ensemble (triangles).

Whereas there does not appear to be much change in the extreme water levels through time, the number of surge and setdown events increase with time in concordance with an increase in number of open water days. The number of surge and setdown events, relative to the 25th and 75th climatological quantiles (calculated from the 30-year 1980 to 2010 time series) increased at a rate of 0.13 events per day of increase in the open water season during the hindcast period ($R^2 = 0.77$; $pval < 0.05$; Figure 3.1b). Extending the time series out to 2050, the trend increases to an additional 0.15 surge events per day of increase in the number of open water days ($R^2 = 0.90$; $pval < 0.05$).

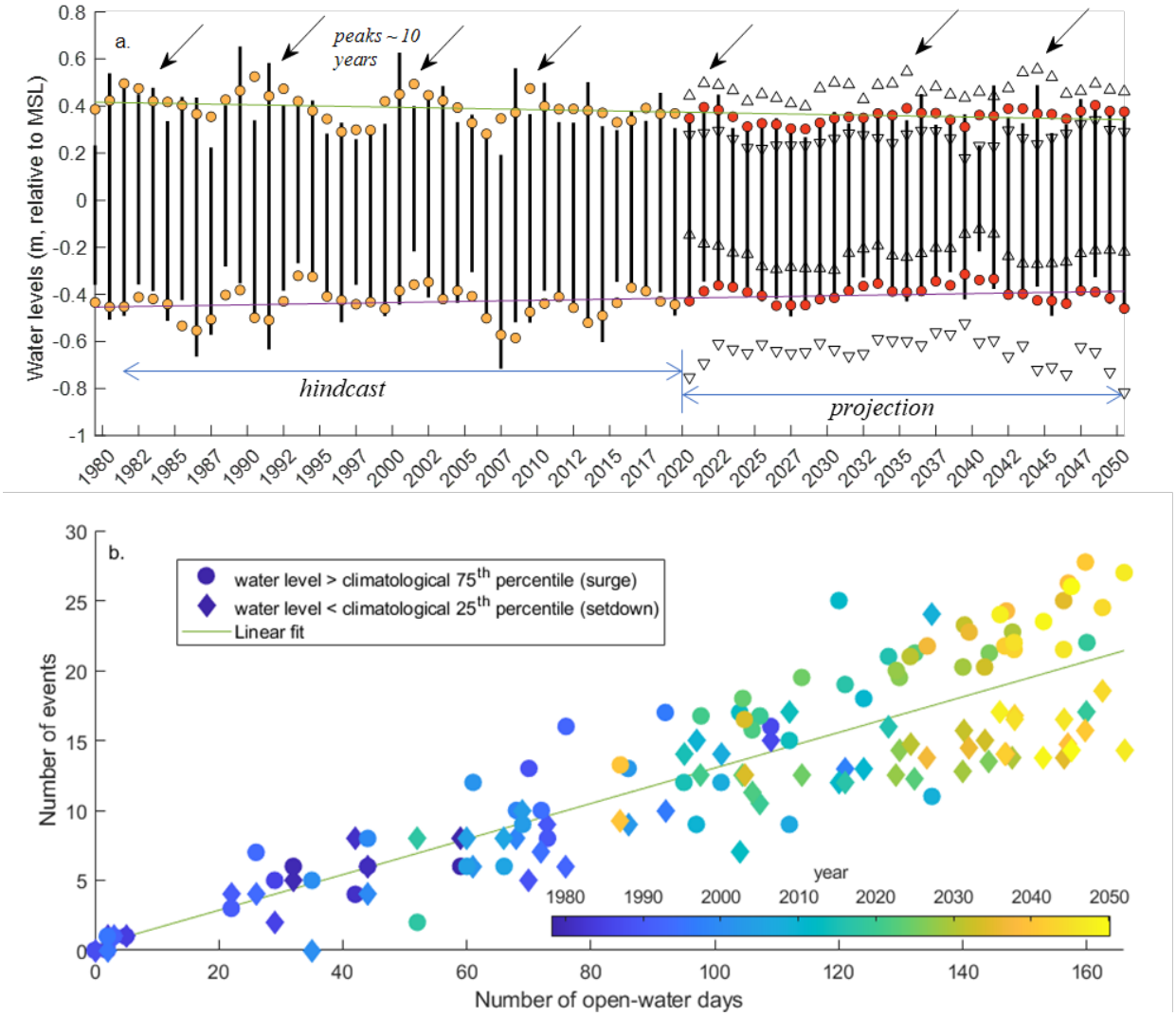

Figure 3.1 Plots showing extreme water level variations and its correspondence to the length of the ice-free season (1979 – 2050).
Time-series plot (a.) showing modeled annual maxima and minima non-tidal residual water levels (vertical bars) in ~20m water depth near the open boundary of the Tier 2C sediment transport model. The range-values (vertical bars) for the projection time period (2020–2050) represent the model ensemble mean of four GCMs (Table 2.1). Colored circles are the 3-year moving means: orange and red for the hindcast and projection time periods, respectively. Upward and downward facing triangles denote the maximum and minimum of each model ensemble. Solid lines are the least-squares fitted regressions (-0.1 cm/year and +0.1 cm/year for the annual maxima and minima, respectively (*p-val*<0.05)). (b.) Scatter diagram showing the annual count of water levels greater than or less than climatological threshold water levels plotted against the number of open water days for the same year. Climatological thresholds are the 75th (5 cm) and 25th (-10 cm) percentile water levels computed from the 30-year hindcast from 1980 to 2010.

3.2 Waves

Waves were simulated with the Tier 2B standalone wave model SWAN (Booij et al. 1999, see Report 1, Section 3.2.2 for details on the wave model). Boundary conditions for the model runs of the hindcast period (1979 – 2019) were provided by ERA5. The projected period (2020 – 2050) was calculated for a model ensemble consisting of four GCMs (Table 2.1; Section 2). The time series were reconstructed for

each ensemble member and wave statistics were calculated separately for each model ensemble member (Section 2.2.1). The ensemble was then calculated as the mean across the members.

For regional patterns in significant wave heights (Figure 3.2), wave heights are only considered for the open water season (when ice cover is less than 15%) since here the focus is on mean and extreme values that can be reached. Otherwise, waves during the closed seasons were considered as having zero wave height, so that the effect of the decreasing sea ice can be more closely investigated. Note that the threshold of sea ice concentrations for defining the open/closed -water season varies somewhat throughout the literature and that in cases when satellite data are used to assess ice concentrations as is done here, a threshold of 15% or greater is preferred as this is the minimum at which space-based measurements give reliable measurements (Strove et al. 2016; Crawford et al. 2021).

3.2.1 Temporal changes in waves

Future wave heights (2020 – 2050) are projected to be slightly larger in Foggy Island Bay compared to the past (1979 – 2019). The differences between the model ensemble wave height projections and the hindcast were calculated for the mean significant wave height, as well as for the 95th and 99.5th percentiles. While differences for the mean wave heights appear to be small, the difference for the 95th percentile reaches roughly 10 cm, primarily in areas inshore of the barrier islands. The differences for the 99.5th percentile reach ~ 20 cm and are more evenly distributed across Foggy Island Bay than for the 95th percentiles. While the difference can partially be attributed to differences in the wind pattern between hindcast and projections (Figure 3.3a.), e.g., more wind coming from a southerly direction for the projections, the continued reduction in sea ice cover (Figure 3.4) appears to be the main cause for the differences. The longer season (Figure 3.4) allows for storms, which are generally stronger in the fall (Figure 3.3b.c), to generate higher extreme wave heights.

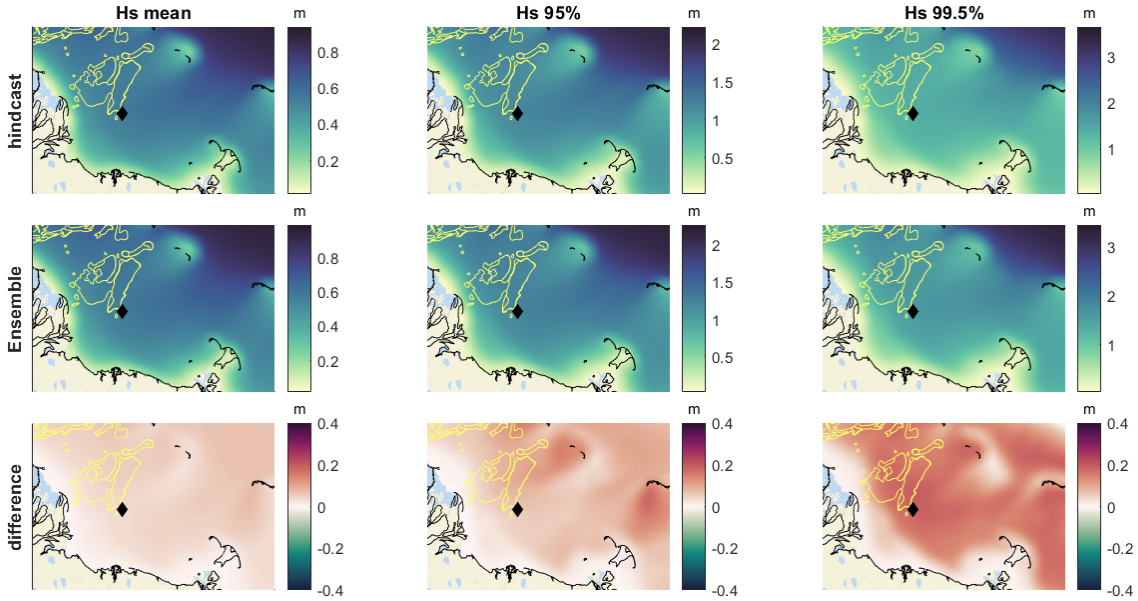

Figure 3.2 Mapped differences between the hindcast (1979–2019) and model ensemble projected (2020–2050) mean, 95th, and 99.5th percentile wave heights within Foggy Island Bay.
The projected wave heights are calculated for the model ensemble from 1979 to 2019 for the hindcast, and from 2020 to 2050 for the projection time period. The Boulder Patch area is shown with yellow outlines. The black diamond indicates the location of the planned artificial island (LDI). The bottom panels show the increase in wave heights between the hindcast and projection.

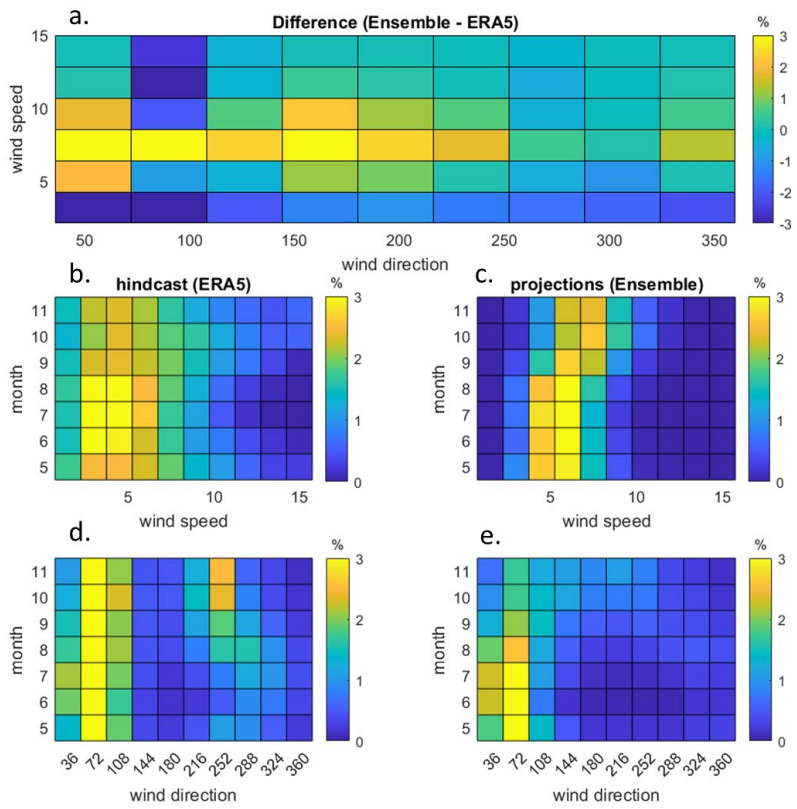

Figure 3.3 Heatmap plots showing the difference in probability of occurrence between projected and hindcasted wind speed and direction.
The difference in occurrence between model ensemble projection and hindcast winds (model ensemble minus ERA5) is shown in (a.). The probability of occurrence is also shown by month (May to November) for wind speed (b.) and direction (d.) during hindcast period (b. and d.) and for the projected period (c. and e.). Wind speed and direction are reported in m/s and degrees from True North.

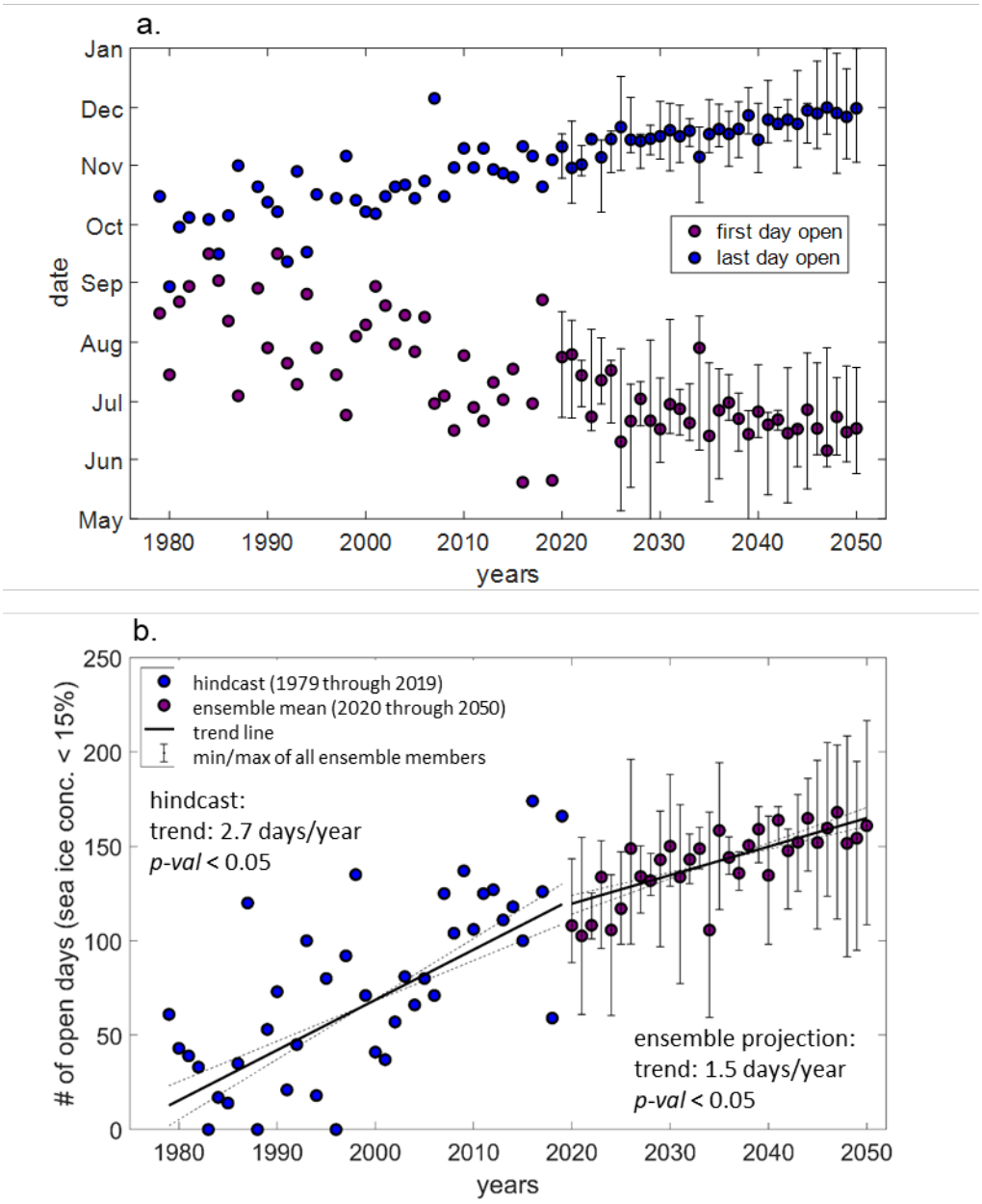

Figure 3.4 Time-series plots showing the number of open water days at Foggy Island Bay from 1979 through 2050.
The hindcast time period is derived from ERA5 data; the projection time period, from 2020 through 2050, and is the mean from all four GCMs (Table 2.1), with error bars indicating the first/last day (a.) or shortest/longest duration (b.) of open water of any the model ensemble members. (a.) The first (purple circles) and last (blue circles) days of the annual open water season. Note that for the hindcast period, the years 1983, 1988, and 1996 were closed throughout the year. (b.) The number of open water days per year and trend lines (solid black lines). Error bars denote the maximum and minimum values of the four-member GCM model ensemble in both plots. Data shown are for ~ latitude 70.5°N and longitude 147.5°W and days when ice cover <15%.

While for the beginning of the hindcast period, the first open day occurred as late as mid-September (1984 and 1991, Figure 3.4a), and some years did not open at all (1983, 1988, 1996). The last years of the hindcast period saw the first day of opening as early as May (2016 and 2019). The model ensemble shows a continued trend in earlier opening (Figure 3.4a). The last day in the open season moved from the end of

September/early October to the end of November for the projected period. Overall, the hindcast period saw an increase in open days of 2.5 days/year, while the model projections show a likely increase in the future of 1.5 days/year (Figure 3.4b).

3.2.2 Local comparison of wave variables

To further investigate the changes in wave parameters over time in the nearshore, we focus on the area of the planned artificial island (LDI). The mean and maximum wave height trends are largest in October for the hindcast period, whereas for the projections the largest trend in mean and maximum wave heights is seen in November (Figure 3.5). Here, wave heights during the ice-covered winter season are considered as having zero wave height. The shift in maximum wave height trends from October for the hindcast to November for the projections is likely caused by the extended open water season of the projections. During the hindcast period, the last day of the open season continuously shifted to a later day in October, effectively allowing for more wave energy in the region, while some years at the beginning of the hindcast period remained quiescent due to ice cover throughout the year (Section 3.2.1, Figures 3.4 and 3.6). The projections indicate that the month of October is ice free (Figures 3.4a), and that the last day of the open season will shift to a later day in November. On the other hand, the smallest increase in the maximum H_s hindcast trend is found for the month of September, when the area was largely ice free (except for 1983). The projections do not show a significant trend for the maximum wave height in September and October, while the mean wave height trend was smallest in September (Figure 3.5a), the month that all model ensemble members indicate as possibly ice-free after 2025 (Figure 3.6c).

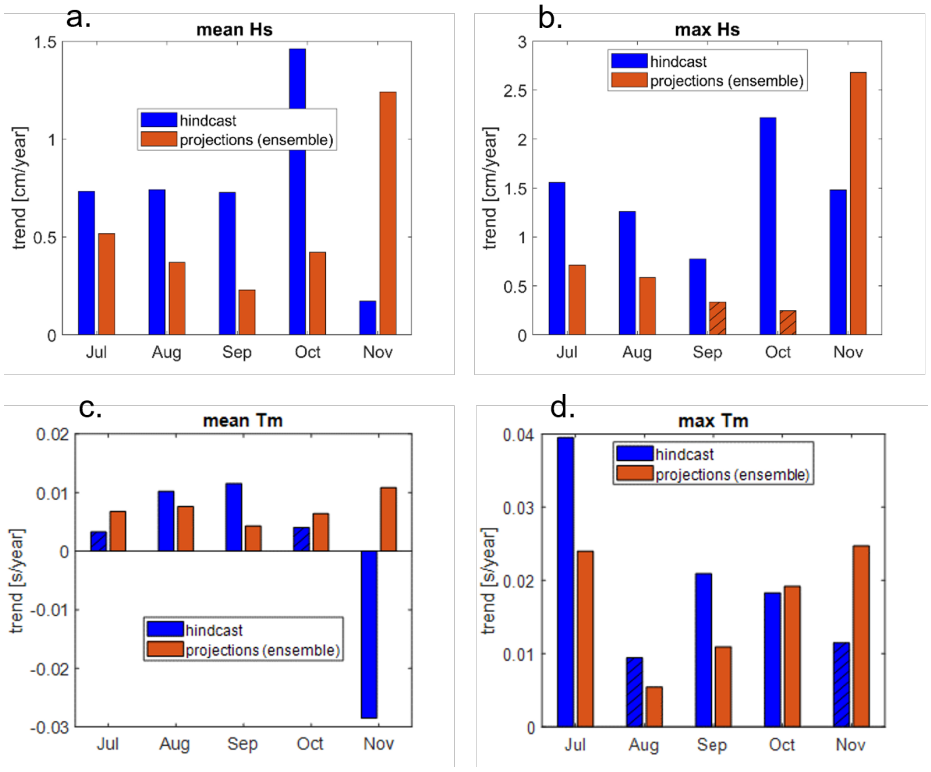

Figure 3.5 Bar plots showing monthly trends of mean and maximum wave heights (a. and b.) and wave periods (c. and d.) for the hindcast and projection time periods at the proposed LDI site shown in Figure 2.2.
Wave heights during the closed season are treated as zero. Hatched bars show no significant trend.

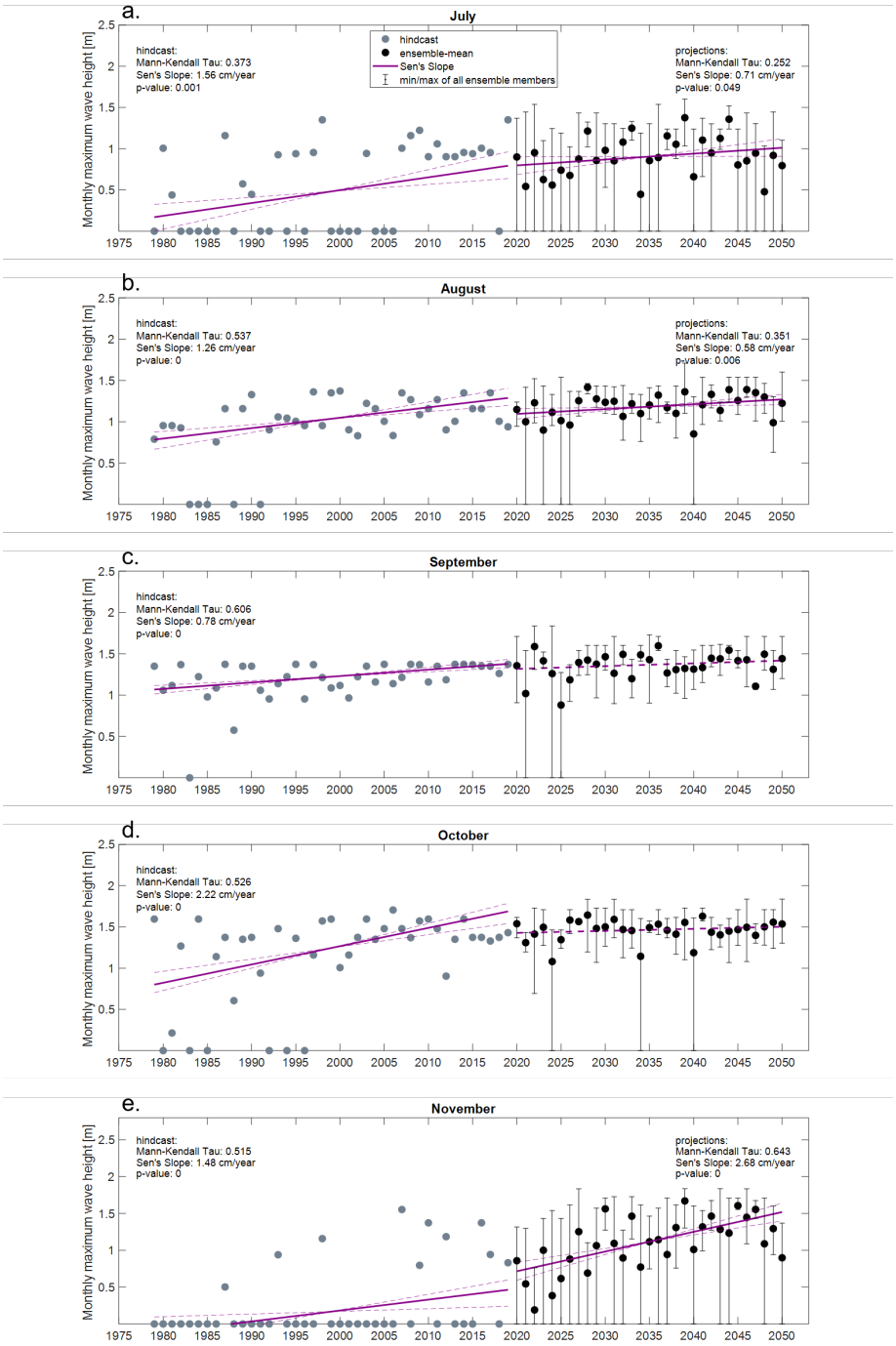

Figure 3.6 Monthly annual local maximum wave heights from 1979 through 2050 at the proposed LDI site shown in Figure 2.2.
Maxima are shown for the open water months July through November (a.- e.). The dashed lines are the uncertainty ranges for a 95th percent confidence interval.

Changes in the mean wave period at the location of LDI are small (around 0.02 s/year), whereas offshore wave periods show a significant increasing trend (around 0.1 s/year, see Table 3.1). Inspection of the

mapped model output of maximum T_m for a month-long simulation in 2019 (Figure 3.7a) shows significant blocking and scattering of swell energy by the barrier islands (note the lower T_m landward of the barrier islands). A comparison of the T_m timeseries at the boundary and inshore observations and model output shows that wave periods are generally lower by as much as ~3 s in the nearshore (Figure 3.7b).

Table 3.1 Monthly trends in T_m at the LDI and offshore of the northern model boundary (N70.4º, W147.5º) for the hindcast and projection time periods

Month	Offshore trend [s/yr]		Nearshore trend (at LDI) [s/yr]	
	Hindcast	Projections	Hindcast	Projections
July	0.11	0.05	0.04	0.02
August	0.10	0.03*	0.01*	0.01*
September	0.06	0.05	0.02	0.01
October	0.13	0.03	0.02	0.02
November	0.09*	0.11	0.01*	0.02

*not a statistically significant trend (*p-val* > 0.05)

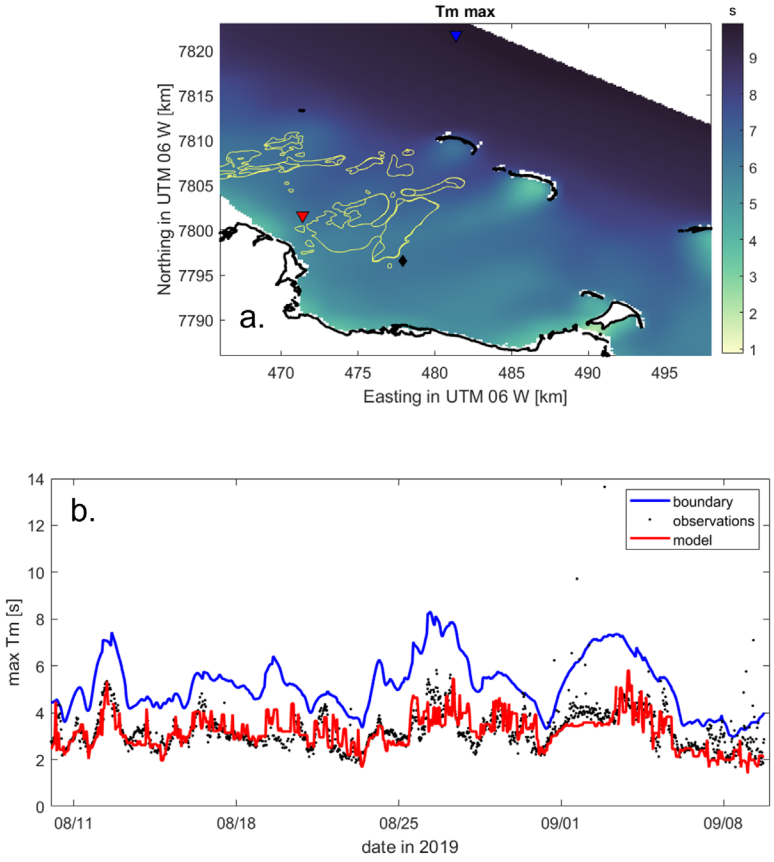

Figure 3.7 Difference in the maximum wave period between offshore boundary and nearshore. Map (a.) shows spatial differences in maximum mean wave periods (max T_m) in the Foggy Island Bay vicinity. The Boulder Patch area is shown as yellow outlines. The black diamond indicates the location of the planned LDI construction; blue/red triangles show locations of time-series comparisons near the boundary (blue triangle), model

output, and observations (both at the red triangle). (b.) Time series comparing the maximum T_m at the northern boundary (blue line) with observations (black dots), and model results (red line) for a period in 2019.

Decadal changes in wave height and wave power (P) were assessed by calculating the mean of hindcasted and projected wave heights from 2010 until 2050 compared to the climatological mean from 1980 through 2009. A weekly moving average was applied to all time series. These values show an almost linear increase from the onset of the ice-free season to the fall season when wave heights decrease rather fast until the sea surface is once again covered with sea ice (Figure 3.8). While part of this pattern can be explained by higher fall season windspeeds, the slow melting of the sea ice and the fast re-freeze shown in Figure 3.8b corresponds to increases and decreases in wave heights, suggesting that this could also be a function of the fetch length. Figure 3.8 shows that while the maximum in the means for each period (0.5 m for 1980-2009, 0.77 m for 2010-2019, 0.57 m for 2020-2029, 0.63 m for 2030-2049) do not show a trend over time, the most striking differences in wave heights can be found in the shoulder seasons (June-July and October to December) due to the increase in the duration of the ice-free period.

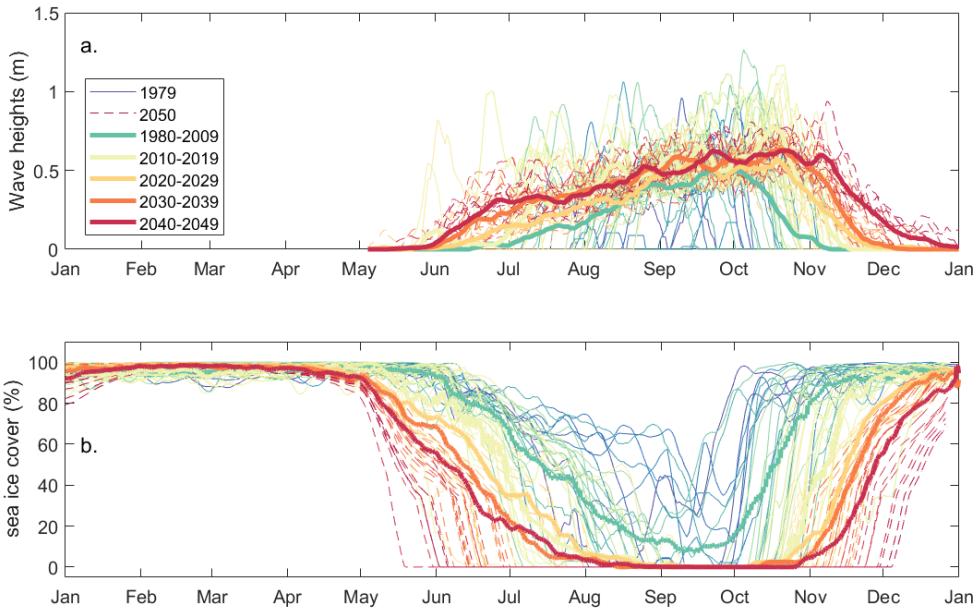

Figure 3.8 Changes in wave heights and corresponding sea ice cover from 1979 through 2049 within Foggy Island Bay and immediate vicinity.
Wave heights (a.) and sea ice cover (b.) are shown for every year (thin lines) through the calendar year while the mean was calculated for the periods 1980–2009, 2010–2019, 2020–2029, 2030–2039, and 2040–2049 (thick lines). The hindcast period (1980–2019) is shown with solid lines whereas the projected period is shown with dashed lines for individual years. All values were calculated with a weekly moving mean. For times of ice cover > 15%, wave heights were set to zero.

The wave power (P, Eq. 3) was calculated for the same time periods as the wave heights. The 99.5th percentile of the wave power shows a similar correlation to the sea ice cover as the wave heights in that it increases most for the months June through July and October through December over time (Figure 3.9). Here, the highest 99.5th percentile of P was found for the period 1980-2009, resulting from a couple of years with higher extreme T_m.

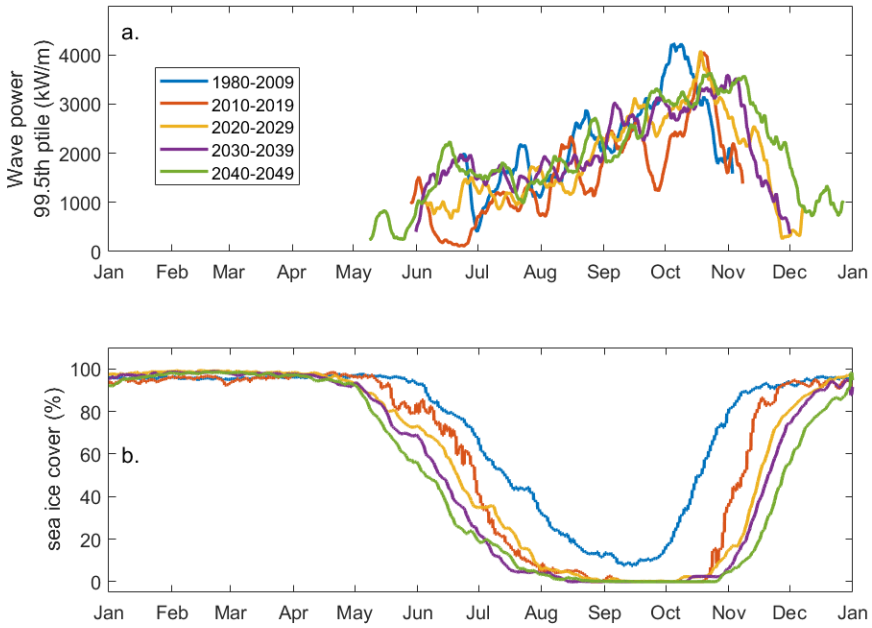

Figure 3.9 Changes in the mean of the 99.5th percentile wave power and corresponding sea ice cover.
The mean of the 99.5th percentile of the wave power (a) and the sea ice cover (b) were calculated for the periods 1980–2009, 2010–2019, 2020–2029, 2030–2039, and 2040–2049. All values were calculated with a weekly moving mean.

3.2.3 Projected changes in return period wave heights

Return periods (RP, or recurrence intervals) were calculated for significant wave heights at the 1-year, 5-year, 10-year and 20-year levels for the hindcast and the projected time periods. The absolute difference in RP wave height values was calculated as the return period for projected wave heights minus hindcasted wave heights. The 1-year RP shows the largest difference (> 0.2 m) between hindcast and projection periods (Figure 3.10), which is in agreement with the larger projected wave heights (Figure 3.2). For the 51year,101year, and 201year RP, this difference is strongest inshore of the barrier islands, especially in the shadow of the barrier islands. This can probably be attributed to the fact that the wind direction has more southwesterly components for the projections (Figure 3.3a), driving more locally wind generated waves instead of waves from a more northeasterly direction, which are blocked by the barriers for the hindcast period. Close to shore, the difference between hindcasts and projections is roughly zero, due to the shallow depth.

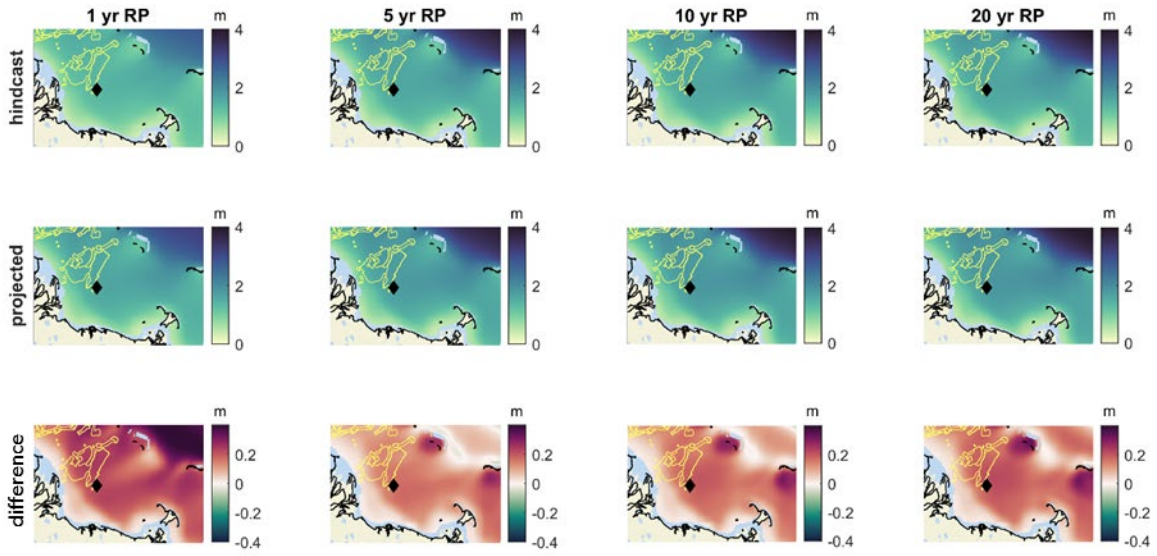

Figure 3.10 Maps showing the hindcast and projected annual, 5-year, 10-year, and 20-year return period wave heights.
The Boulder Patch area is shown as yellow outlines. The black diamond indicates the location of the planned artificial island (LDI). The bottom panels show projected (middle) minus hindcasted return period wave heights (top). Note that NOAA's 2017 Continually Updated Shoreline Product (CUSP) is plotted as the land boundary (black solid line) and that lidar measurements from 2011 were used to demarcate the barrier island morphologies in all model simulations (showing as areas of no waves). The discrepancy in barrier island locations highlights the need for updating the bathymetry and land boundaries in both hindcast and model projection simulations.

3.3 Sediment-transport potentials (vector fields)

Sediment transport patterns within Foggy Island Bay were modeled with the coupled wave-hydrodynamic-sediment transport model Tier 2C. The model was run with representative sea states to assess the sediment transport potentials for the entirety of the 40-yr hindcast and 30-yr projection time periods (Section 2.1; Nederhoff et al. 2023). Representative sea states and their probability of occurrence during the hindcast and projection time periods were identified using clustering techniques on continuous time series. A total of 31 different combinations of waves, surge, and wind were identified to optimize computational costs (Section 2.2.2). The same coupled wave-hydrodynamic-sediment transport model was also run as a continuous time series for month-long time periods. That application was to assess the effect of transport under sea-ice and the influence of riverine sediment inflows (presented in this section).

3.3.1 Sea states

Representative sea states at the open boundary of the Tier 2C model, and derived from an equivalent of 160 years of hourly data (see Section 2.2.2), are listed in Table 3.1. In total, 31 sea states were defined, 15 states which cause a set-down of the water level due to easterly direct winds (blowing from the east), 15 states which cause a setup due to westerly winds (blowing from the west), and one sea state which represents no sediment mobility when ice cover is greater than 15% or wave heights are smaller than 0.50 m. The 1 sea state that represents no sediment mobility was not explicitly run. The probability of all the sea state combined results in a total probability of 1.

Each of the 30 representative sea states were run for four days. The first day was used for model spin-up. Day two through four for the actual simulation. All simulations use a triangle shape storm hydrograph (as was done by Callaghan et al. 2009) where the peak is reached after 2.5 days of simulation.

Table 3.2 Parameter values of 30 representative sea states used in this study

Sea state #	Wave height (m)	Mean wave period (s)	Wave direction (degrees from True North)	Surge (m aboveMSL)	Wind speed (m/s)	Wind direction (degrees from True North)
1	0.67	3.8	148	-0.24	12.9	17
2	0.73	3.4	220	0.35	12.8	224
3	0.79	5.1	328	0.32	4.6	272
4	0.81	4.9	39	-0.37	4.8	79
5	0.81	3.9	279	0.39	6.7	275
6	0.83	4.5	76	-0.37	6.0	79
7	1.34	4.5	160	0.28	13.6	7
8	1.50	4.3	227	0.26	12.9	228
9	1.51	4.9	284	0.46	10.3	266
10	1.52	5.7	322	0.37	8.2	275
11	1.52	6.0	44	-0.54	7.1	76
12	1.56	5.3	75	-0.39	9.3	82
13	2.22	6.7	323	0.42	11.3	280
14	2.23	5.2	237	0.27	14.2	232
15	2.25	5.6	274	0.55	13.1	252
16	2.25	6.8	45	-0.45	8.8	86
17	2.28	6.1	75	-0.47	12.0	83
18	2.91	6.2	281	0.58	15.0	259
19	2.98	7.8	326	0.49	15.3	106
20	3.01	7.3	48	-0.40	12.4	97
21	3.01	6.8	75	-0.60	14.1	83
22	3.74	8.4	332	0.42	15.9	134
23	3.76	8.0	47	-0.42	14.4	119
24	3.76	7.6	74	-0.56	16.0	84
25	3.79	7.0	277	0.62	16.9	261
26	4.42	8.1	77	-0.59	17.4	89
27	4.45	8.8	50	-0.46	16.4	174
28	4.53	10.2	340	0.60	17.5	130
29	5.19	10.1	358	0.15	18.9	173
30	5.28	8.9	81	-0.48	18.8	91

A representative example of a wind-driven setup situation is sea state #10 (Figure 3.11a, Table 3.2). Wind speeds reach 8.2 m/s and come from the west (275°). The result is wind-driven setup of about 37 cm

relative to MSL. The consequence is flooding of the ebb-tidal delta in the western part of the model domain. Moreover, an alongshore current from west to east is being generated as a result of the wind direction.

A representative example of a wind-driven setdown situation is sea state #11 (Figure 3.11b, Table 3.2). Wind speeds reach 7.1 m/s and come from the east (76°). The result is a wind-driven setdown of in this case -54 cm. Offshore wave heights reach 1.5 m. Again, we see an alongshore current being generated that follows the wind direction. In this case, it is a ~1 m/s east-west alongshore flow.

To visualize pathways and understand sediment connectivity we utilized a novel Lagrangian sediment transport model data post-processor referred to as SedTRAILS (Sediment TRAnsport vIsualization & Lagrangian Simulator; Pearson et al. 2021). SedTRAILS is used to visualize the magnitude (length of the arrow) and direction of transport of each sea state in Figure 3.12. The panels show dominant alongshore transport, either toward the east or west, depending on wind and incident wave direction. An eddy forms in the southeast section of Foggy Island Bay when relatively strong winds (>12 m/s) blow from the north in opposition to waves coming from the southeast (sea states 1 and 7).

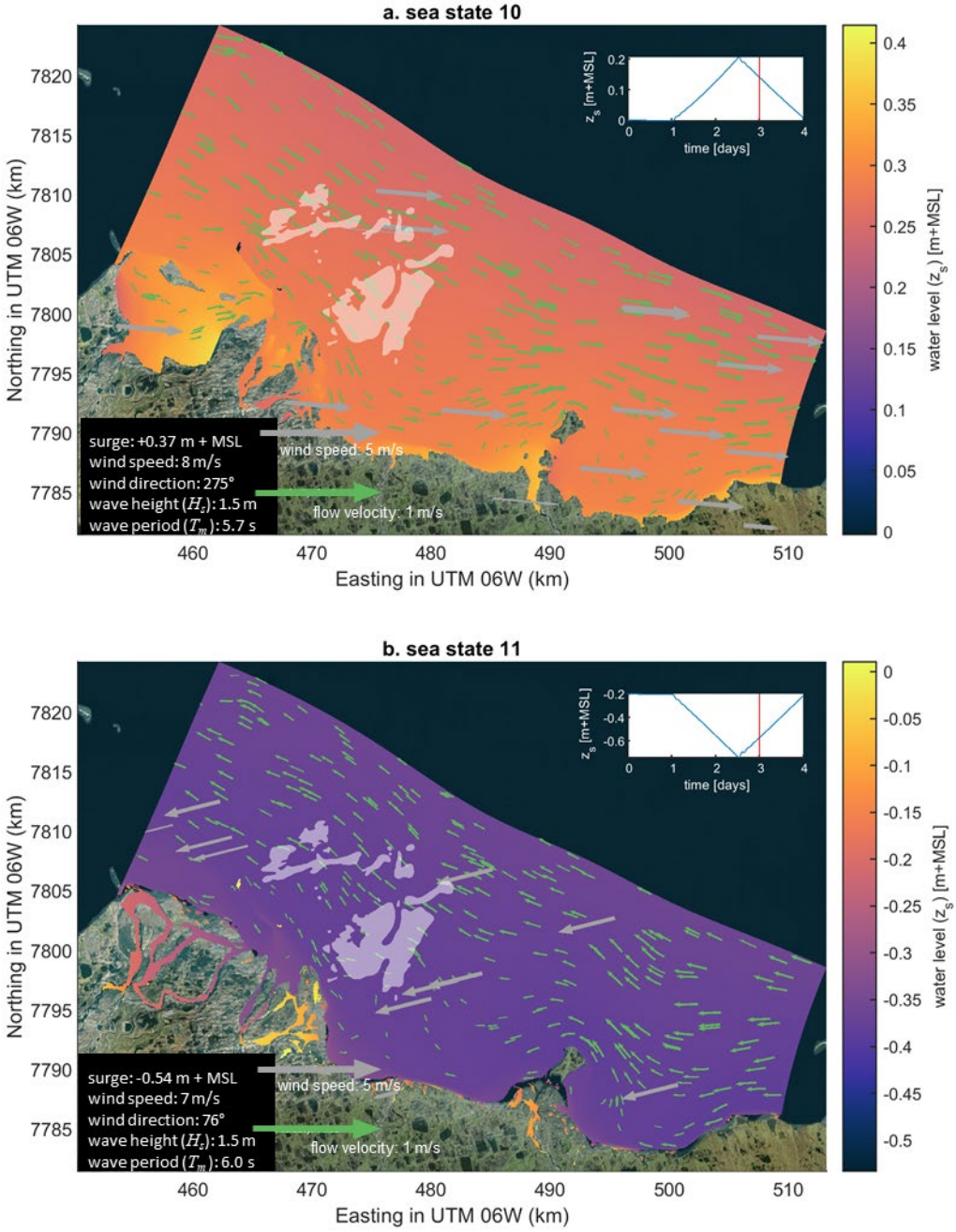

Figure 3.11 Maps of modeled outputs at a snapshot in time of two example sea states.
An example output from a wind-driven setup event (sea state #10) is shown in (a.) and for a wind-driven setdown event (sea state #11) in (b.). Text in lower left corner of each panel provides details of the particular sea state. Right-side upper insets show the parameterized stormtide (non-tidal residuals plus tidal amplitude) time series and instant in time of the map output (red vertical line).

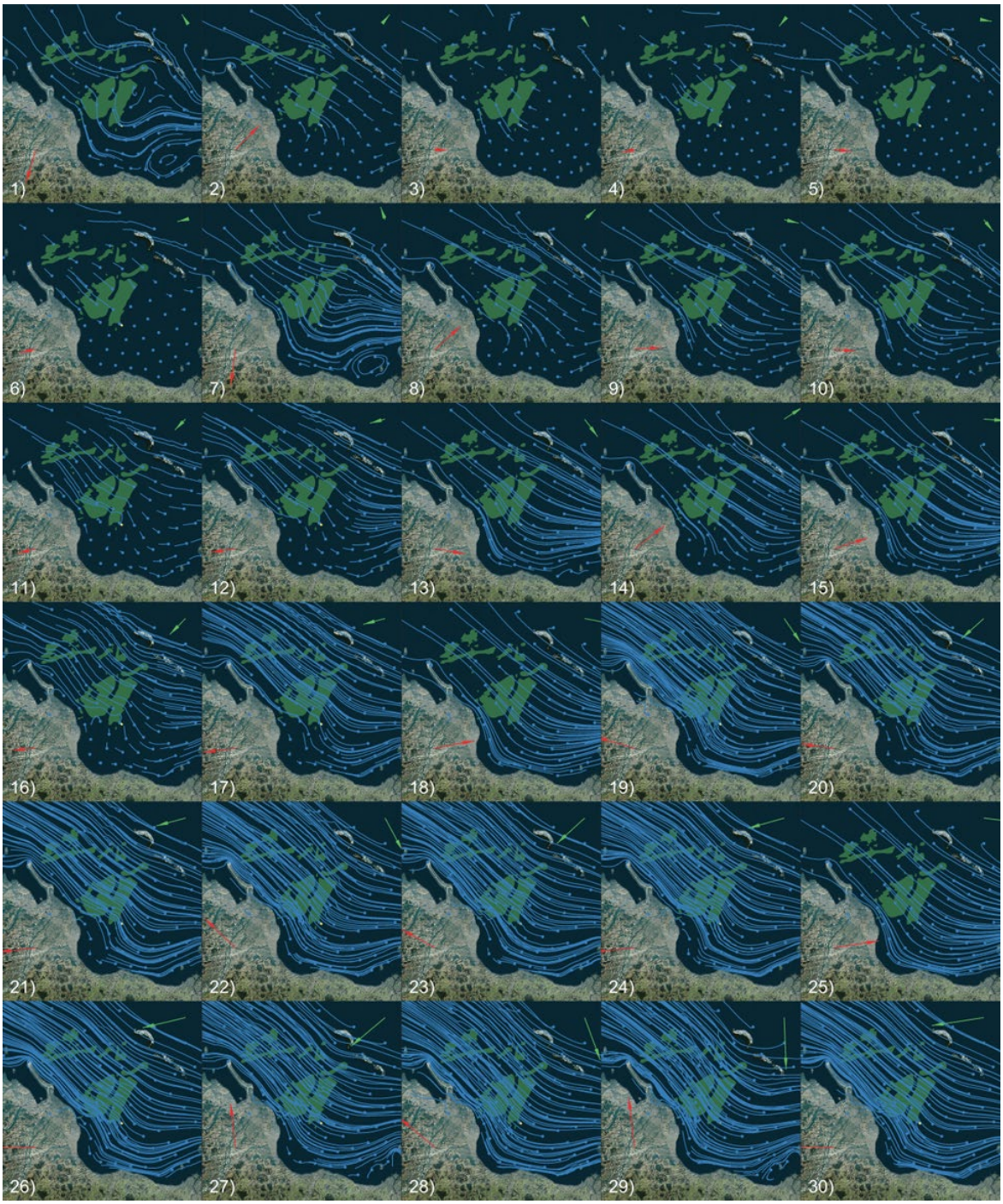

Figure 3.12 Mapped sediment transport potentials as visualized with SedTRAILS for the 30 identified representative sea states.
Blue arrows indicate sediment transport potentials, with the point intended to illustrate an initial starting point of a virtual sediment particle. Red and green arrows indicate the wind speed applied across the domain and waves applied at the open boundaries of the model domain. Magnitude and direction are depicted by the length and direction of the arrows. Corresponding sea states applied at the open boundaries of the model are listed in Table 3.2.

To obtain total net mean transport fields over the hindcast and projected time periods, results from each sea state are multiplied by their probability of occurrence. Computed probability occurrences of each sea

state and model are listed in Table 3.2. The probability of all sea states combined equals one (100%), including sea state 31 (not shown), which represents negligible sediment mobility due to landfast ice or quiescent wave and stormtide conditions. Thus, the sum of all sea state probabilities represents the percent of time when conditions are considered sufficient to move sediments: 13% for the 40-year ERA5 hindcast, and 16%, 14%, 52%, 30% and 28% for the CNRM, ECEarth, GFDL-CMIP5, HadGemSST, and model ensemble 30-year projections, respectively.

Table 3.3 Occurrence probabilities (0 to 1) of each sea state and model.

Sea state #	ERA5	CNRM	EC-Earth	CMIP5-GFDL	HadGem-SST	Ensemble
1	4.72E-04	1.20E-03	5.23E-04	4.29E-03	5.04E-04	1.63E-03
2	2.11E-03	3.39E-03	1.38E-03	3.79E-03	1.60E-03	2.54E-03
3	1.02E-02	2.15E-02	9.02E-03	7.27E-02	4.83E-02	3.79E-02
4	1.68E-02	2.19E-02	1.29E-02	1.44E-01	5.13E-02	5.76E-02
5	1.06E-02	1.01E-02	1.34E-02	1.50E-02	1.52E-02	1.34E-02
6	4.64E-02	4.21E-02	5.55E-02	8.71E-02	8.50E-02	6.74E-02
7	2.88E-05	1.47E-05	1.10E-05	0.00E+00	0.00E+00	6.44E-06
8	3.89E-04	2.32E-04	5.15E-05	1.25E-04	1.07E-04	1.29E-04
9	3.04E-03	3.50E-03	2.57E-03	2.68E-03	4.79E-03	3.39E-03
10	8.90E-04	7.48E-03	1.41E-03	2.20E-02	1.17E-02	1.06E-02
11	2.91E-03	7.71E-03	2.75E-03	8.01E-02	1.59E-02	2.66E-02
12	2.02E-02	2.17E-02	2.49E-02	3.30E-02	3.74E-02	2.93E-02
13	6.48E-05	2.45E-03	1.47E-04	3.72E-03	9.24E-04	1.81E-03
14	2.16E-05	0.00E+00	0.00E+00	0.00E+00	0.00E+00	0.00E+00
15	7.28E-04	4.01E-04	4.31E-04	1.25E-04	2.02E-04	2.90E-04
16	2.74E-04	2.40E-03	6.07E-04	2.69E-02	2.68E-03	8.14E-03
17	9.18E-03	1.12E-02	8.45E-03	1.15E-02	1.52E-02	1.16E-02
18	5.76E-05	6.99E-05	2.58E-05	1.93E-05	3.68E-05	3.79E-05
19	0.00E+00	3.42E-04	4.42E-05	2.22E-04	3.53E-04	2.40E-04
20	7.56E-05	6.73E-04	1.80E-04	4.42E-03	3.83E-04	1.41E-03
21	3.32E-03	3.10E-03	3.41E-03	5.66E-03	3.96E-03	4.03E-03
22	0.00E+00	4.05E-05	0.00E+00	0.00E+00	4.78E-05	2.21E-05
23	1.80E-05	3.61E-04	0.00E+00	9.27E-04	6.62E-05	3.38E-04
24	1.05E-03	8.24E-04	3.57E-04	1.05E-03	7.54E-04	7.47E-04
25	4.32E-05	0.00E+00	0.00E+00	0.00E+00	3.68E-06	9.20E-07
26	5.26E-04	2.76E-04	4.78E-05	0.00E+00	1.21E-04	1.11E-04
27	0.00E+00	6.26E-05	0.00E+00	0.00E+00	0.00E+00	1.56E-05
28	0.00E+00	3.31E-05	0.00E+00	0.00E+00	0.00E+00	8.28E-06
29	0.00E+00	1.47E-05	0.00E+00	0.00E+00	0.00E+00	3.68E-06
30	1.37E-04	0.00E+00	0.00E+00	0.00E+00	0.00E+00	0.00E+00

ERA5 in column 2 is for the 40-year hindcast (1980–2019); columns three through six are for the four 30-year individual model projections (2020–2050), Column seven is the model ensemble mean of columns two through five. Cell shading denotes relative scaling of low (no color) to high (red) values.

3.3.2 Hindcast model runs (ERA5)

Model results of each individual sea state are combined into one single mean transport field. The probability of sediment mobility for the 30 sea states equals 0.13 for the hindcast model runs. In other words, 87% of the time, we assume no sediment transport due to low wave heights, negligible currents, and/or ice cover.

Overall mean transport rates show a predominant alongshore transport from east to west (Figure 3.13a). Alongshore sediment transport rates computed along shore-perpendicular transects that extend from shore to the landward side of the barrier island chain are estimated to range between 12 and 38 m^3/m/day. Transport rates at the east and west ends of Foggy Island Bay are more than twice as fast compared to the approximate center of Foggy Island Bay, resulting in deposition and erosion along the east and west flanges of Foggy Island Bay, respectively (Figure 3.13a). Extending seaward from the Endicott causeway, transport rates again decrease, resulting in overall deposition immediately west of Foggy Island Bay. A similar pattern is seen for silt and clay sediment classes (Figure 3.13d,e). These classes have the highest transport potentials and contribute each to about half of the alongshore transport. Pebbles rarely move (Figure 3.13b) whereas sand is more onshore directed (Figure 3.13c). We estimate a net cross-shore transport into Foggy Island Bay of 5.6 m^3/m/day for all sediment fractions combined.

Model simulations indicate that the construction of LDI (sited at E477,914, N7,796,601, UTM zone 06W; Hilcorp Alaska, LLC, May 2017) will locally influence hydrodynamics, waves, and consequent sediment transport patterns. The construction is expected to cause some shadowing of the predominant alongshore-directed east to west current and, during times of higher wave conditions, wave shadowing on the leeside of the structure (southwest to southeast of the structure, depending on incident wave directions). Considering the entirety of the time period, there is a net adjustment in the transport direction and magnitude immediately northwest of the structure (Figure 3.14). Sediment transport potentials decrease slightly and rotate clockwise in the near vicinity and rotate slightly counterclockwise far-field across the southern end of the Boulder Patch (Figure 3.14b).

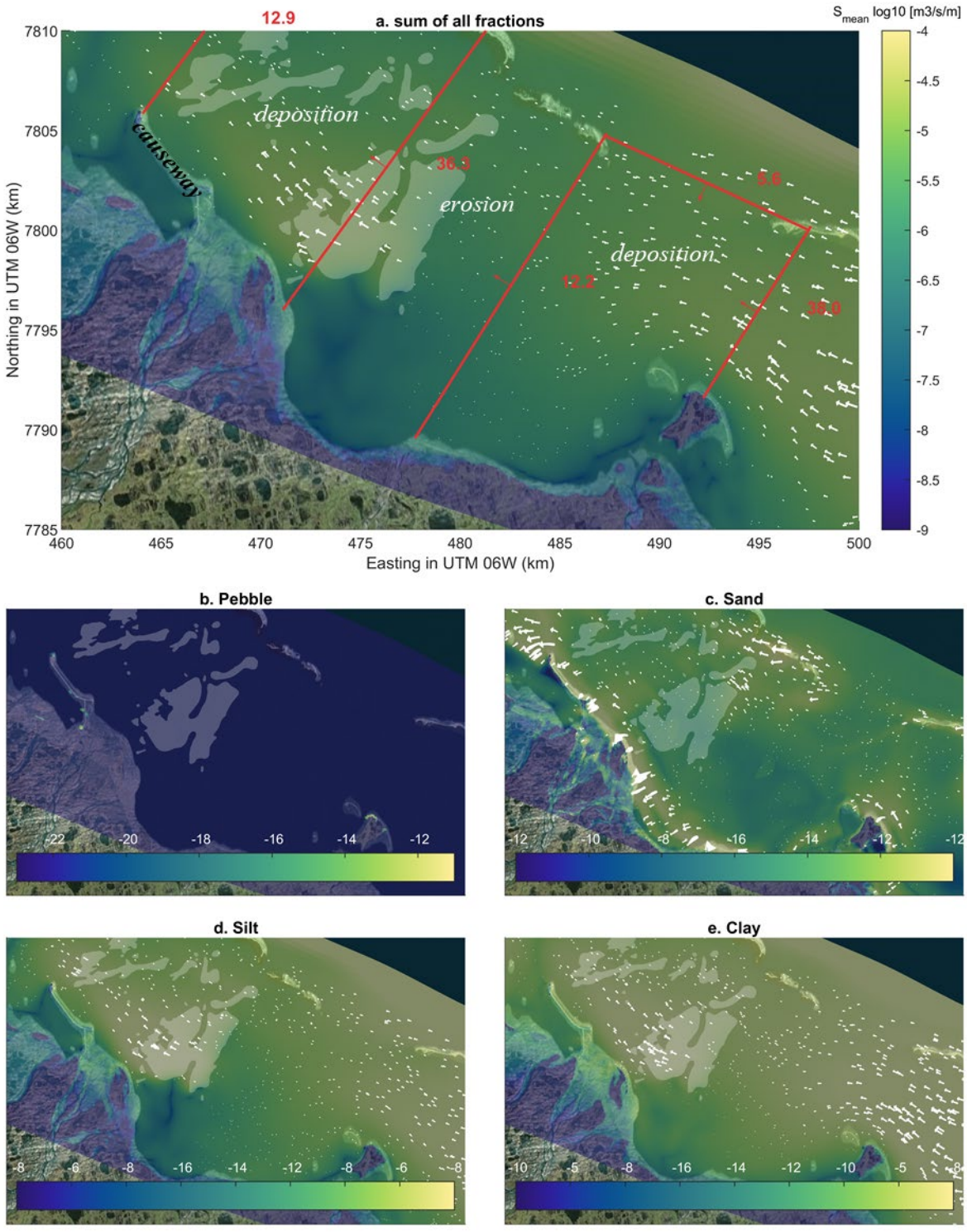

Figure 3.13 Maps showing mean transport potentials per sediment class for the hindcast period, without LDI.

The color bar denotes the sediment transport rate ($m^3/s/m$) with the logarithmic range varying by sediment class. Directions and relative magnitudes are shown with the white curved arrows. Panel (a) shows the combined sum of all sediment fractions. Red lines denote arbitrarily drawn transects across which net

transport of all fractions for the entire hindcast period are computed ($m^3/m/day$). Overall deposition and erosion patterns, as deduced from transport across the shore-perpendicular transects, are identified with white text. (b-e) Mean transport potentials for pebbles (b), sand (c), silt (d), and clay (e).

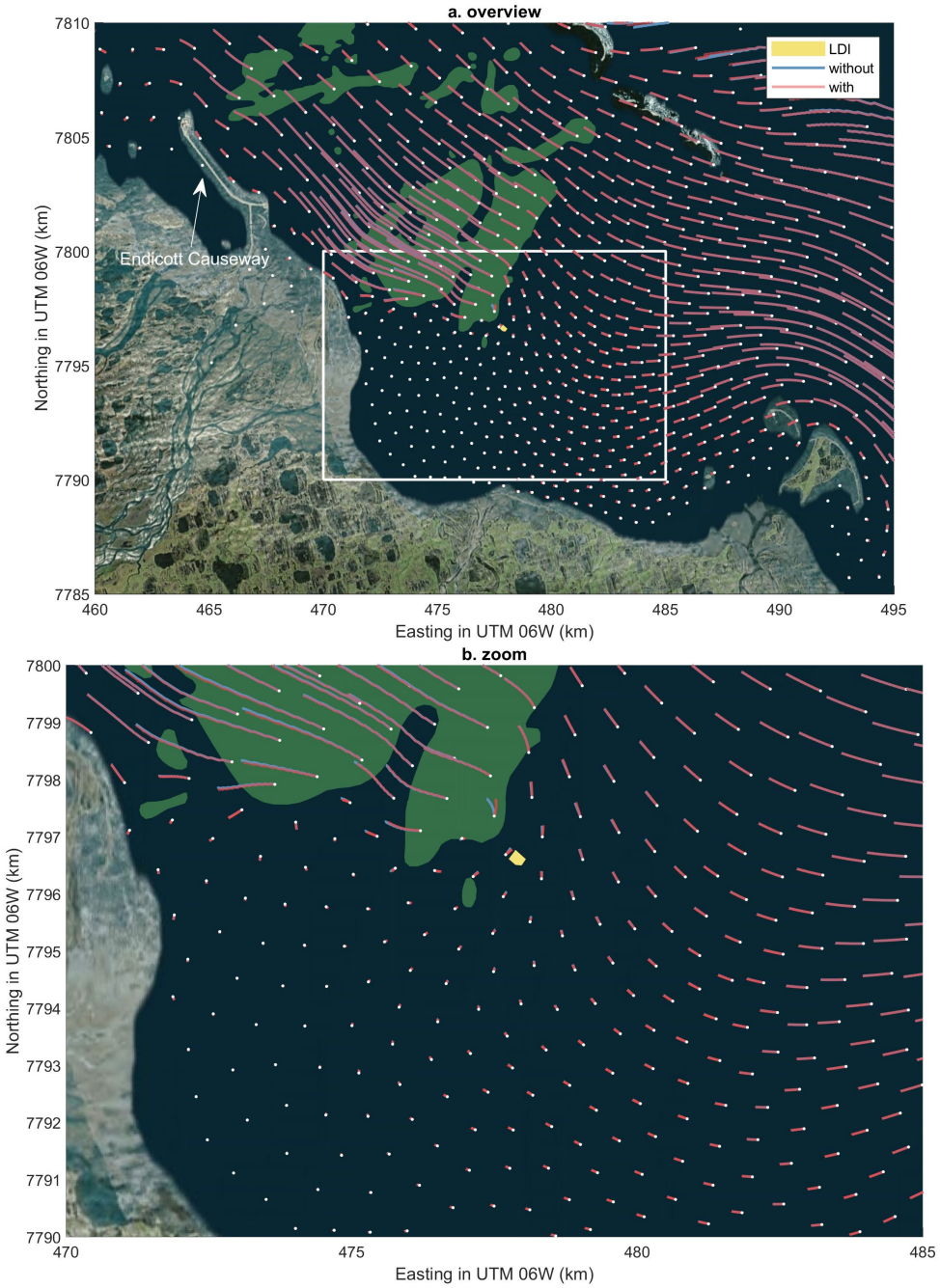

Figure 3.14 Maps showing mean sediment transport potential as visualized with SedTRAILS for model simulations without (red) and with the LDI in place (blue).
Red and blue curved lines indicate directions of sediment transport potentials, with the points intended to illustrate an initial starting location of a virtual sediment particle. Panel (a.) shows the mean sediment transport potentials across Foggy Island Bay, while panel (b.) shows a close-up as indicated in (a.) by the white rectangle. The Boulder Patch areas are indicated in green, and the proposed LDI construction location in yellow.

3.3.3 Projected sediment transport potentials

One of the strengths of the sea state approach is that it relatively straightforward to re-run the analysis for other probabilities of wind, wave, and surge levels, due to climate change. Here we find that the probability of occurrence of the 30 sea states (Table 3.2) equals 0.28 for the 4-member GCM ensemble covering years 2020–2050; more than a double increase from that of the hindcast period (total probability of 0.13). In other words, the total amount of time when oceanographic conditions are considered capable of moving sediments is expected to increase to 28% for the 30-year future period compared to 13% of the time during the 40-year hindcast.

Projected changes in sediment transport patterns are mostly concentrated near the largest boulder patch (Figure 3.15). Results from the model ensemble indicate a counterclockwise change in direction and an overall increase in transport magnitudes (longer red lines in Figure 3.15b). For the GCM ensemble, the alongshore and cross-shore transport magnitudes increase by 14 to 57% (Figure 3.17f).

An analysis between the GCM models (CNRM, ECEarth, GFDL-CMIP5 and HadGemSST) shows significant inter-model variability but that three of the four GCMs consistently indicate large changes in sediment transport magnitudes compared to the hindcast (Figure 3.16). GFDL-CMIP5 shows the largest change in magnitude (Figure 3.16d), followed by HadGemSST (Figure 3.16e). Smallest changes are simulated with the ECEarth GCM (Figure 3.16c).

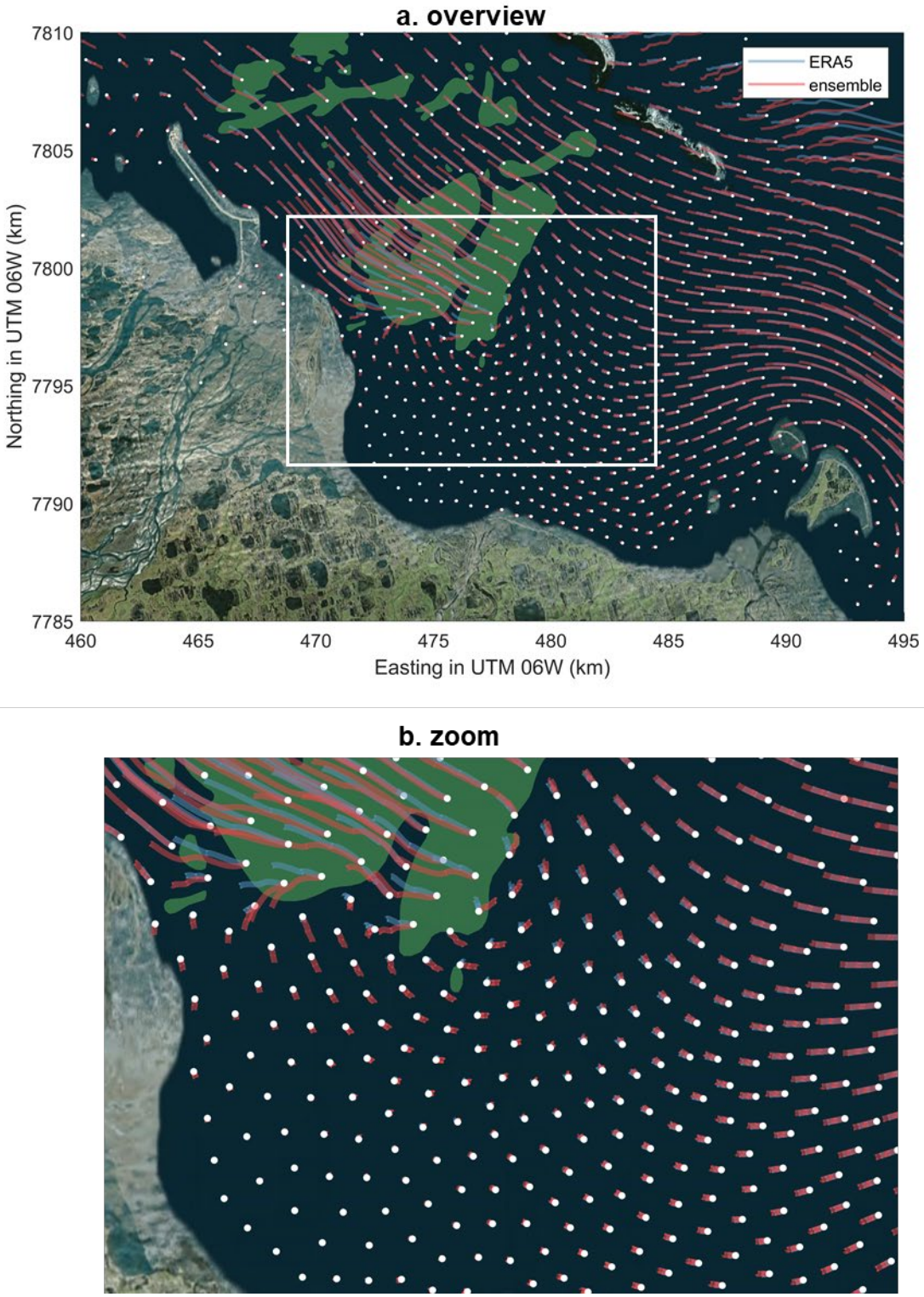

Figure 3.15 Mapped comparisons of the mean sediment transport potentials for the hindcast and projection time periods as visualized with SedTRAILS.
The projected transport potentials are computed from the model ensemble. All simulations assume no LDI construction. Red and blue curved lines indicate directions of sediment transport potentials, with the points intended to illustrate an initial starting location of a virtual sediment particle. Panel (a.) shows the mean sediment transport

potentials across Foggy Island Bay, while panel (b.) shows a close-up as indicated in (a.) with the white rectangle. The Boulder Patch areas are indicated in green.

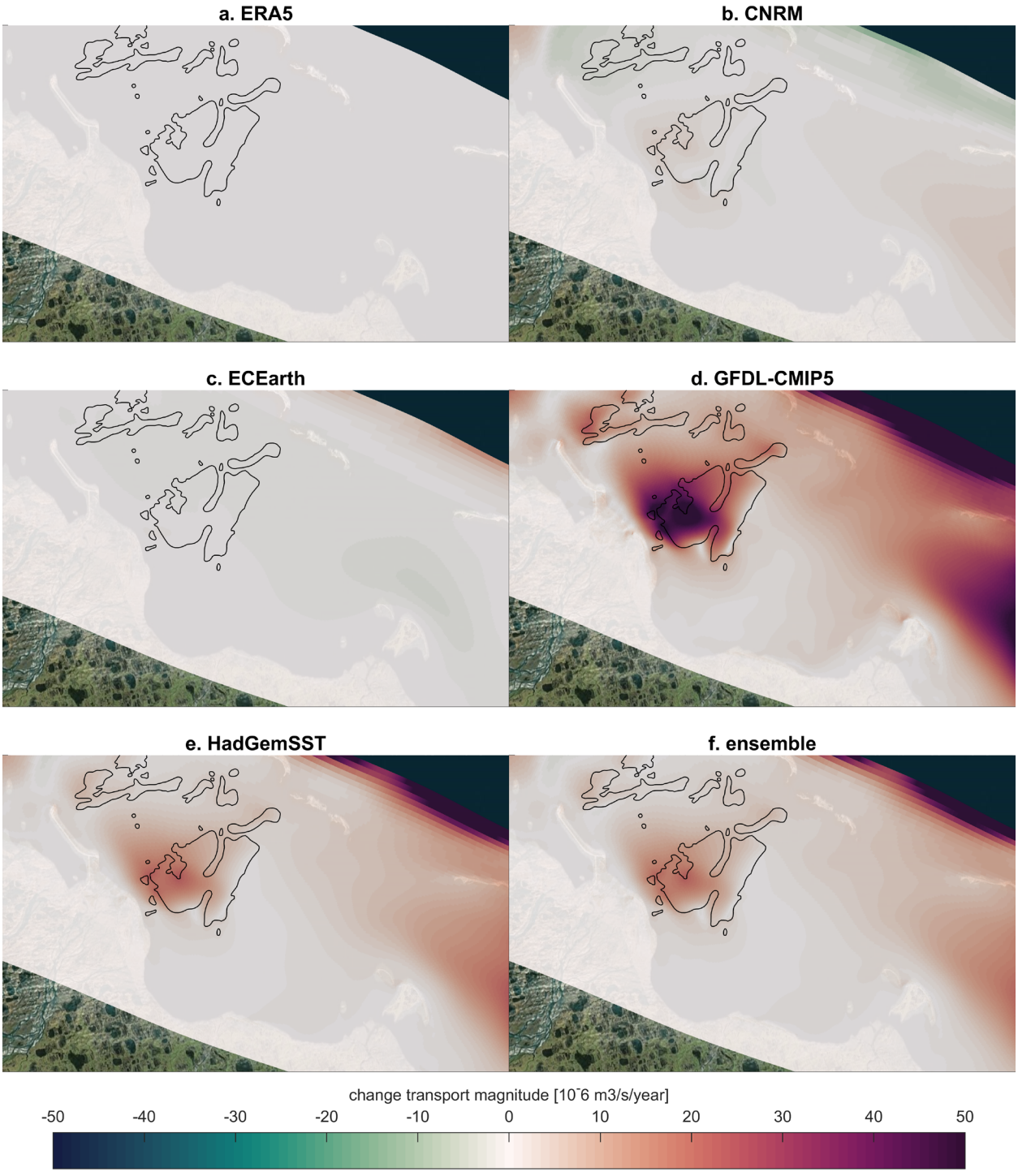

Figure 3.16 Maps showing the percent change in mean transport potentials projected with each GCM compared to the hindcast time period.
All simulations are without the LDI in place.

One of the potential negative effects of the structure is sedimentation/erosion across the Boulder Patch. To gain insight to the impacts of the construction on the Boulder Patch, the net erosion/deposition at each patch was calculated with and without the LDI in place. Model simulations without the construction indicate a net average erosion rate of -9 cm per year across all patches (Figure 3.17b). Half of the patches exhibit erosion. Boulder patch #15 has the largest erosional trend with 50 cm/year· m^2 (possibly due to being on the lee side of the larger boulder patch #11). When comparing the situation with and without the LDI, minor differences emerge, except at patch #13 (Figure 3.17c), a small area immediately southwest of the LDI (#13; yellow). The model indicates a net erosional trend at patch #13 prior to construction and reverses to a net depositional environment of +11 cm/year/m^2, post-construction. Deposited and eroded material in the area consists mainly of silt and clay.

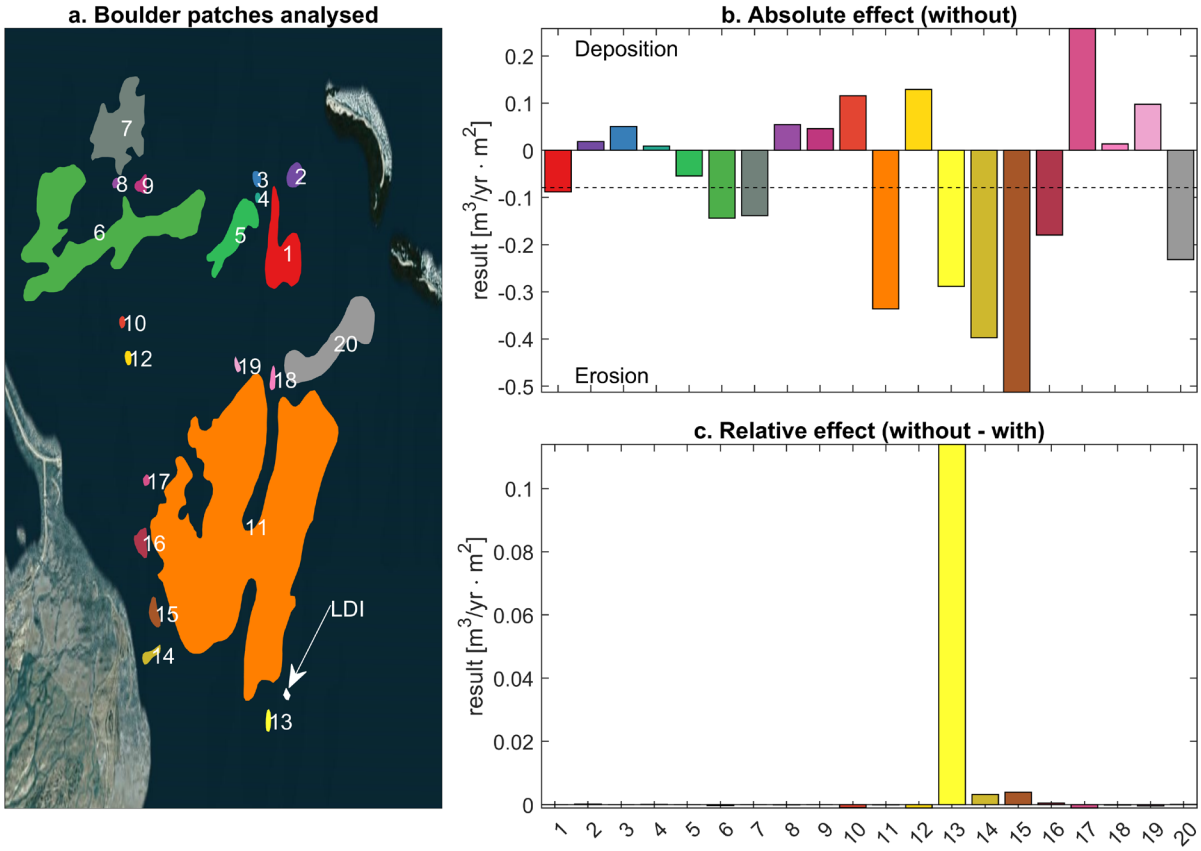

Figure 3.17 Analysis of net sediment erosion and deposition with and without the LDI in place for the model ensemble projection (2020–2050).
(a.) Map showing color-coded boulder patches. (b.) Bar graph of the 'background' sedimentation/erosion trends at individual boulder patches, without the LDI construction in place. (c.) Change in net sedimentation/erosion with the LDI construction in place. The horizontal axis on the right-hand panels refers to the individual color-coded boulder patches shown in (a.).

3.3.4 Transport of a fluvial sediment plume

In a separate continuous (i.e., brute force) simulation, sediment from the Sagavanirktok River was simulated with and without ice cover. Simulations of currents and sediment transport under sea ice were done using an ice-module beta-version. The ice-module is based on the approach from Semtner (1976) for which space and time-varying ice concentration and thickness maps are additional inputs. Ice is treated as

a floating structure exerting pressure on the water column, with the same time step as the hydrodynamic FLOW model. Delft3D4 developments are ongoing for inclusion of ice drift velocity, growth, and decay and as such were not explicitly modeled. For these experimental simulations of stream discharge under the sea ice, a contiguous ice cover of 2 m thickness was assumed. In regions with water depths less than 2 m deep, ice was considered attached to the seabed, except at the river mouths where the ice map was thinned to allow for fluvial and sediment discharge outward toward the deeper waters. Simulations were done for a 21-day discharge event from June 1 to 22, 2001, releasing almost 40,000 m^3 of sediment (assumed to be cohesive) and a maximum peak freshwater discharge of 300 m^3/s (Trefry et al. 2005; BP Exploration 2017; Trefry et al. 2009). Model simulations resulted in the material mainly staying within the river channels, but some material was transported to the coastal area (Figure 3.18). In the simulation with complete sea ice cover, the sediment concentration footprint extends about the same distance offshore as the scenario without sea ice but is not dispersed as far toward the west. The difference is due to lower along-shore currents for the under-ice simulation and greater sediment stirring in response to waves for the simulation without sea ice.

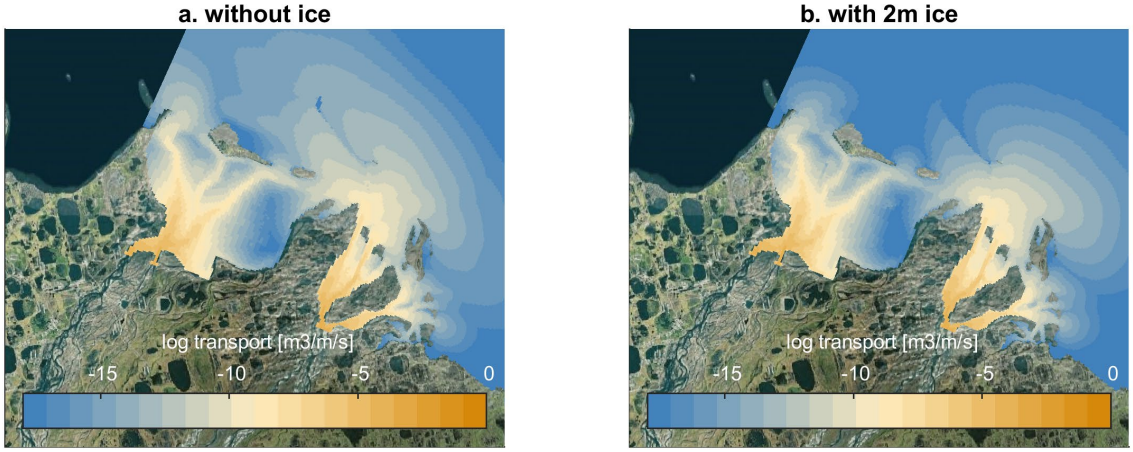

Figure 3.18 Maps showing maximum modeled transport of an assumed cohesive fluvial discharge plume under sea ice and without sea ice cover.
Panel a: without sea ice cover. Panel b: with sea ice cover.

4 Conclusions and future directions

The research described in this report presents findings of projected changes in oceanographic conditions within the nearshore region of Foggy Island Bay in Stefansson Sound and additionally the influence of the planned construction of Liberty Drilling Island (LDI) on sediment transport pathways during the design-life of that project (here taken to be 2020–2050). The results are derived from a suite of numerical models that include dynamic downscaling from global and regional scales to the local level. The local-level wave model resolves wave propagation and growth across a 200 m resolution grid that includes blocking and scattering effects by barrier islands located approximately 20 km offshore. For simulations of sediment transport, a coupled wave-flow model was developed that hosts a 50 m resolution hydrodynamic flow and transport grid. Model details and validations are presented in Report 1 (Kasper et al. 2022) of this 2-part report series.

4.1 Waves within Foggy Island Bay

Time series of modeled waves indicate that the 99.5th percentile and annual return period projected wave heights over the 2020–2050 time period are expected to be on the order of 20 to 30 cm higher, on average, throughout Foggy Island Bay compared to the hindcast (1979–2019). Change metrics vary within the bay (Figure 3.2) due to the offshore wave energy being highly modified by the barrier islands as well as depth-induced saturation due to bottom friction and whitecapping that affect both wave energy from offshore and local wave growth (Raubenheimer et al. 1996; Nederhoff et al. 2022). While some of the difference might be attributable to changes in wind patterns, the increase is strongly correlated to the longer open water season, which expanded by 2.5 days/year between 1979 and 2020 and is projected to continue but at a slightly slower rate of 1.5 days/year between 2020 and 2050 (Figure 3.4). Note that here and throughout, the projection results are based on a model ensemble average of four separate climate model projections of the unmitigated RCP8.5 scenario. In this study, we selected the higher emission scenario because limited resources only allowed for exploration of one scenario and selecting the higher member is more conservative, and because observations and model evidence point to the RCP 8.5 trajectory as being very likely by 2041–2060 (IPCC 2021, Box B.1.2). The difference between using RCP 8.5 versus lower scenarios is likely to yield similar results as there are minimal differences between emission scenarios during the first half of the 21st century; deviations between the scenarios are substantially larger beyond 2050 (see, for example, Figure SPM.8 in IPCC 2021). Wave power density, a metric that combines wave periods and the square of wave heights, showed marked correspondence to percent sea ice cover within the model grid. Throughout the year, monthly annual extreme (99.5th percentile) wave power increases approximately linearly from the onset of the ice-free season to the fall season, when wave power decreases quickly until the sea surface is once again covered with sea ice (Figure 3.9). While part of this pattern can be explained by higher fall season windspeeds, the slow melting of the sea ice, and the fast re-freeze, corresponds to increases and decreases in wave power, suggesting that the milder slope in the increase of wave power, compared to the steeper decrease in slope of the wave power during the fall months, could also be a function of the fetch length. Comparing decadal patterns in Figure 3.9, a most striking differences is seen in the extension of wave energy during the shoulder seasons (June-July and October to December) with, for example, wave power extending well into the month of December by 2040-2049, compared to 1980–2009 when the region was free from any wave power due to the presence of sea ice. Interestingly, the highest 99.5th percentile wave power was found in October 1980–2009, resulting from a couple of years with higher extreme wave periods.

Computed trends from modeled wave time series at the LDI location were found to be statistically significant during both the hindcast and projection time periods and for nearly all months analyzed (July through November). The November monthly mean and maximum wave heights are projected to increase at a rate of 1.2 and 2.7 cm/year, respectively. These rates are 50 and 80% higher than what was found for the same month during the hindcast period and clearly reflects the continuing delay in annual sea ice freeze-up.

For all other months, the inverse is true, such that the trends are greater for the hindcast compared to the projection time period (Figure 3.5). While not substantiated, we speculate that the reason for the higher trends in hindcasted July through October wave heights compared to the projections is because of the rapid increase in number of open water days during the hindcast period and continued realization of no ice cover during these months going forward in time.

Mean and maximum wave periods (relevant to wave steepness, wave runup, and seabed sediment mobilization) were also found to trend upward during both the hindcast and projection time periods (except the November hindcast time period). However, trends were found to be small (<0.04 s/year), especially compared to offshore conditions where trends are on the order of 0.10 s/year. Inspection of modeled output fields and wave spectra indicate that the difference is again due to diffraction of wave energy by the barrier islands and blocking of swell energy from reaching the shallows of Foggy Island Bay (Figure 3.7).

4.2 Sediment Transport Potentials

Suspended and bed load transport of both cohesive (silt and clay) and non-cohesive sediment (sand and pebbles) were simulated. Because simulation of multi-decadal long sediment transport potentials in Foggy Island Bay necessitated the build of a numerical model with coupled wave and hydrodynamic processes across high-resolution model grids (50 to 200 m) that covered nearly 3,000 km^2; it was computationally unfeasible to continuously model all the hindcast and projection scenarios that together equated to ~160 years. For example, the runtime for a month-long 3D simulation on a 3.8 GHz 30-core machine takes roughly 30 hours. Therefore, input-reduction techniques that characterize the full range of wave, flow, and wind forcing conditions were used.

Sea states were defined by 31 combinations of wave heights, mean wave periods, mean incident wave directions, maximum/minimum non-tidal residual water levels, wind speeds, and wind directions (Table 3.2). Fifteen sea states cause a setdown due to easterly winds, and 15 sea states cause a setup due to westerly and onshore-directed winds. One sea state represents no sediment mobility when ice cover is greater than 85% or wave heights are smaller than 50 cm. The probability of all the sea states combined results in a total probability of 1. An advantage of the sea state approach is that it is relatively straightforward and quick to compute and estimate mean sediment transport potentials for different time periods and forcings, as long as the frequency of occurrence of each sea state at the open boundary of the model is known.

Mean transport rates are found to be mainly alongshore from east to west (Figure 3.12), with an estimated rate of 12 – 38 m^3/m/day for the hindcast. Transport rates at the east and west ends of Foggy Island Bay are more than twice as fast compared to the approximate center of Foggy Island Bay, resulting in deposition and erosion along the east and west flanges of Foggy Island Bay, respectively (Figure 3.13a). The results compare well with measured bathymetry changes between 2018 and 1945/53 that showed similar patterns of deposition and erosion (Report 1, Figure 2.2). Model results indicate that along-shore occurrence of transport potentials may double for the projection time period. Silt and clay exhibit the highest transport potentials and contribute each to about half of the alongshore transport. Pebbles barely move whereas sand is transported primarily cross-shore, presumably resulting from mobilization by waves and transport by wave-driven, tide, and non-tidal residual currents. Net cross-shore rates are estimated to be on the order of 5.6 m^3/m/day into Foggy Island Bay for the hindcast and with an increase of 58% for the model ensemble projection.

The model ensemble projection is based on four climate realizations (i.e., downscaled GCMs), each of which show varying degrees of change with respect to the hindcast. Three of the four GCMs show at least a doubling in the magnitude of transport at the coast and in the shallows of eastern Foggy Island Bay

(Figure 3.17). One of the GCMs indicates very little to no change in transport except along small sections of the coast. All four GCMs indicate an overall increase in transport potentials when the entirety of Foggy Island Bay is considered.

Near the planned construction site of the LDI (Hilcorp Alaska, LLC, 2017), all GCMs show a clockwise change in direction compared to the hindcast. Across the ecologically important Boulder Patch, directions remain consistent and only the magnitude of the sediment transport potential changes.

To visualize pathways and understand sediment connectivity we utilized a novel Lagrangian sediment transport model data post-processor referred to as SedTRAILS (Sediment TRAnsport vIsualization & Lagrangian Simulator; Pearson et al. 2021). The presence of the island causes some shadowing of the predominant alongshore directed east to west currents and wave shadowing on the lee side of the structure (southwest to the southeast of the structure, depending on incident wave directions). A possible result of these changes is an increase of the magnitude and counterclockwise rotation of the transport direction across an adjacent Boulder Patch region west of the LDI (Figure 3.14b). Model simulations without the LDI indicate that half of Boulder Patch areas experience net erosion, with an overall mean of -3.2 cm per year for the hindcast period (not shown) and -9 cm per year for the projection (Figure 3.17b). Introducing the LDI into the future simulations affects the Boulder Patch immediately south and to the west. The greatest impact appears to be on the patch immediately to the south of the LDI. With the construction in place, the erosional tendency of that Boulder Patch has an expected net accumulation of +11 cm per year (i.e., reducing the erosion rate).

Potential generation and transport of excess suspended sediments during construction of LDI was evaluated by Coastal Frontiers (2014). They found that construction activities, which are anticipated to take place in winter, will likely advect sediment under the sea ice and potentially across regions of the Boulder Patch. During the assumed open water season of the subsequent summer following construction of the LDI, side slope grading and armor installation is to continue. Coastal Frontiers concluded that the open water conditions that are expected to exist at the time will allow waves to winnow fine-grained sediments from the gravel fill and that variable wind- and wave-driven currents will disperse the suspended sediments. Along the pipeline alignment which will connect the LDI to the mainland, a backfill mound protruding above the ambient seafloor is anticipated. As waves and currents erode the backfill mound those sediments are also expected to be advected into the Boulder Patch area, comparable to regions identified in this study. Coastal Frontiers conclude that the excess suspended sediment resulting from degradation of the backfill mound are expected to have the largest negative impacts on Boulder Patch kelp productivity.

4.3 Future directions

A test case of the coupled wave-hydrodynamic numerical model's ability to simulate the fate and transport of a spring freshet (discharge) via the Sagavanirktok River was conducted. The simulations cover a 21-day discharge event that released nearly 40,000 m^3 of assumed cohesive sediment in 2001. Simulations that assumed complete ice cover resulted in a plume, driven solely by under-ice currents, that extended roughly 10 km offshore and covered an area of roughly 40 km^2. The extent of this plume is about half of what was measured by Dunton et al. (2005). Running the same simulation without sea ice cover, and thus allowing for wind and wave-driven currents to act on the plume, nearly doubled the area of influence (Figure 3.18). The inconsistency between measured and modeled plume extents indicates a need for some additional physics to be resolved with the model. We hypothesize that accounting for buoyancy, by 'turning on' salinity to reflect true conditions of freshwater inflows to saline waters, will significantly improve the results. Open boundary time series of vertical salinity and temperature gradients would be needed; to this end, results from the Beaufort Sea regional circulation model by Curchister et al. (2017) could potentially be used to develop such parameterizations for different seasons and conditions

(spring break-up, fall freeze-up, wind-setup, and setdown events). We also hypothesize that the simple model schematization of ice effects (pressure-driven lid) on the water column is insufficient and requires further development.

Another point for future work relates to the initial bed composition. In this study, bed composition was derived by interpolating a suite of seabed grab samples that were analyzed for relative sediment concentrations (silt, clay, sand, and pebble/gravel) and sediment grain size (see Section 2 in Report 1 for more details). Following the concepts outlined by van der Wegen et al. (2011), we sought to find an equilibrium initial bed composition map, one that would remain relatively constant under typical conditions, and to test the overall sensitivity of the initial bed composition map on resulting sediment transport potentials. To this end, we repeatedly simulated a single year with increasing morphological acceleration factors. The acceleration factor was used to mimic several years of morphological development. Sensitivity testing revealed that higher acceleration factors resulted in lower sediment transport rates but that no equilibrium sediment bed map could be achieved. We also found that the variations of the initial bed composition strongly affected transport rates. Thus, we believe that the results of this study could be improved by better constraining the uncertainty bands associated with variations of the bed composition.

In this study, we assessed potential changes of waves, hydrodynamics, and sediment transport pathways by comparing results from five individually downscaled GCMs (assuming the RCP 8.5 'business as usual' scenario) and the model ensemble to that of a hindcast. Spatial patterns of change are found to be similar, but the magnitudes differ substantially amongst the models. Inter-model variability and uncertainty is not unusual (e.g., Morim et al. 2019), and therefore the preference is to rely on a model ensemble, as was done here. To further decrease the uncertainty, a larger ensemble, as well downscaling of alternate lower emission scenarios (e.g., RCP2.6) and an evaluation of each model's ability to simulate local historical conditions, would benefit the study.

Lastly, it is important to keep in mind that all simulations assumed the persistent presence of offshore barrier islands as measured with lidar in 2011 (Gibbs and Richmond 2017; Hamilton et al. 2021). Whereas the barrier islands are highly ephemeral (changing orientation, breach locations, and generally migrating westward and onshore; e.g., ~500 m southwest between 2005 and 2020), they continue to mitigate wave energy entering Foggy Island Bay. However, the continued persistence or migration of these features in the coming decades is unknown and currently understudied. Considering the strong influence of these features on the wave climate, sediment transport conditions, and working conditions in Foggy Island Bay, it is suggested that future work include studies to better understand the dynamics and fate of the barrier islands.

5 References

Barnes EA, Dunn-Sigouin E, Masato G, Woollings T. 2014. Exploring recent trends in northern hemisphere blocking. Geophysical Research Letters. 41(2):638-644.

Bieniek PA, Bhatt US, Walsh JE, Rupp TS, Zhang J, Krieger JR, Lader R. 2016. Dynamical downscaling of era-interim temperature and precipitation for Alaska. Journal of Applied Meteorology and Climatology. 55(3):635-654.

Bieniek PA, Erikson L, Kasper J. 2022. Atmospheric circulation drivers of extreme high water level events at Foggy Island Bay, Alaska. Atmosphere. 13(11).

Booij N, Ris RC, Holthuijsen LH. 1999. A third-generation wave model for coastal regions: 1. Model description and validation. Journal of Geophysical Research: Oceans. 104(C4):7649-7666.

BP Exploration (Alaska) Inc., Liberty Development Project Development and Production Plan. Environmental Impact Analysis. Attachment A. Figure 2.5-2. April 2007.

Callaghan DP, Roshanka R, Andrew S. 2009. Quantifying the storm erosion hazard for coastal planning. Coastal Engineering. 56(1):90-93.

Camus P, Méndez FJ, Losada IJ, Menéndez M, Espejo A, Pérez J, Rueda A, Guanche Y. 2014. A method for finding the optimal predictor indices for local wave climate conditions. Ocean Dynamics. 64(7):1025-1038.

Cayan DR, Maurer EP, Dettinger MD, Tyree M, Hayhoe K. 2008. Climate change scenarios for the California region. Climatic Change. 87(S1):21-42.

Chang EKM, Guo Y, Xia X, Zheng M. 2013. Storm-track activity in IPCC AR4/CMIP3 model simulations. Journal of Climate. 26(1):246-260.

Coastal Frontiers Corporation. 2016. 2015-2016 Freeze-up study of the Alaskan Beaufort and Chukchi Seas. Final Report. CFC-962/963. Prepared for Shell Offshore Inc. and U.S. Dept. of the Int., Bureau of Safety and Environmental Enforcement. Funded in part by BSEE Contract E15PC0002. 225 pp.

Crawford A, Stroeve J, Smith A, Jahn A. 2021. Arctic open-water periods are projected to lengthen dramatically by 2100. Communications Earth & Environment. 2(1):109.

Curchitser, EN, Hedstrom, K, Danielson S, Kasper J. Development of a Very High-Resolution Regional Circulation Model of Beaufort Sea Nearshore Areas. U.S. Dept. of the Interior, Bureau of Ocean Energy Management, Alaska OCS Region, Anchorage, AK. OCS Study BOEM 2018-018. 81 pp. 2017.

Dunton K, Funk D, Iken K. 2005. Long-term monitoring of the kelp community in the Stefansson Sound Boulder Patch: Detection of change related to oil and gas development. Report Alaska Minerals Management Service. (2005):39.

Dunton KH, Schonberg SV. 2000. The benthic faunal assemblage of the boulder patch kelp community. In: Truett JC, Johnson SR, editors. The natural history of an arctic oil field: Development and the biota. Boston: Academic. p. 371–397.

Engelstad AC, Erikson LH, Reguero BG, Gibbs AE, Nederhoff K. In press. Generating nearshore wave time-series with a numerical wave model-derived database along the outer coast of Alaska. U.S. Geological Survey Open-File Report. DOI:

Engelstad AC, Erikson, LH, Reguero, BG, Gibbs, AE, Nederhoff, K. In press. Nearshore wave time-series along the coast of Alaska computed with a numerical wave model. Menlo Park, CA, USA: US Geological Survey Data Release. DOI: 10.5066/P931CSO9

Erikson LH, Morim JM, Hemer M, Young I, Wang XL, Mentaschi L, Mori N, Semedo A, Stopa J, Grigorieva V et al. 2022. Global ocean wave fields show consistent regional trends between 1980 and 2014 in a multi-product ensemble. Comunications Earth and Environment. 3(1).

Eyring V, Bony S, Meehl GA, Senior CA, Stevens B, Stouffer RJ, Taylor KE. 2016. Overview of the coupled model intercomparison project Phase 6 (CMIP6) experimental design and organization. Geoscientific Model Development. 9(5):1937-1958.

Gibbs AE, Richmond BM. 2017. National assessment of shoreline change—summary statistics for updated vector shorelines and associated shoreline change data for the north coast of Alaska, U.S.-Canadian border to Icy Cape. Menlo Park, CA: U.S. Geological Survey. Open-File Report 2017-1107.

Gōda, Yoshimi, Hideaki Takeda, and Yoshiichi Moriya. Laboratory investigation on wave transmission over breakwaters. Port and Harbour Technical Research Institute, 1967. PARI Report 000-13-01.

Hamilton AI, Gibbs AE, Erikson LH, Engelstad AC. 2021. Assessment of barrier island morphological change in northern Alaska. Menlo Park, CA: U.S. Geological Survey. Open-File Report 2021–1074.

Hansen JE, Elias E, List JH, Erikson LH, Barnard PL. 2013. Tidally influenced alongshore circulation at an inlet-adjacent shoreline. Continental Shelf Research. 56:26-38.

Hersbach H, Bell B, Berrisford P, Hirahara S, Horányi A, Muñoz-Sabater J, Nicolas J, Peubey C, Radu R, Schepers D et al. 2020. The ERA5 global reanalysis. Quarterly Journal of the Royal Meteorological Society. 146(730):1999-2049.

Hilcorp Alaska, LLC. Liberty development project. Development and production plan. Amendment 3. Report submitted to Bureau of Ocean Energy Mangement, Alaska OCS Region, Anchorage, AK. Submitted on May 26, 2017, by Hilcorp Alaska, LLC, 3800 Centerpoint Dr. Anchorage, AK. 268pp.

Hirahara S, Balmaseda MA, Boisseson E, Hersbach H. 2016. 26 sea surface temperature and sea ice concentration for era5. Eur Centre Medium Range Weather Forecasts, Berkshire, UK, ERA Rep Ser. 26.

IPCC. Summary for Policymakers. In: Climate Change 2021: The Physical Science Basis. Contribution of Working Group I to the Sixth Assessment Report of the Intergovernmental Panel on Climate Change [Masson-Delmotte, V., P. Zhai, A. Pirani, S.L. Connors, C. Péan, S. Berger, N. Caud, Y. Chen, L. Goldfarb, M.I. Gomis, M. Huang, K. Leitzell, E. Lonnoy, J.B.R. Matthews, T.K. Maycock, T. Waterfield, O. Yelekçi, R. Yu, and B. Zhou (eds.)]. 2021.

Kasper J, Erikson LH, Ravens T, Bieniek, P, Engelstad A, Nederhoff K, Duvoy P, Fisher S, Petrone Brown E, Yaman M, Reguero B (University of Alaska, Fairbanks and Anchorage, AK; U.S. Geological Survey, Santa Cruz, CA; Deltares-USA; University of California Santa Cruz). 2023. Central Beaufort Sea wave and hydrodynamic modeling study. Report 1: Field measurements and model development. Anchorage (AK): U.S. Department of the Interior, Bureau of Ocean Energy Management. 100 p. plus Appendices. Report No.: OCS Study BOEM 2022-078. Contract No.: M17AC00020 and IAA No. M17PG00046.

Lesser GR, Roelvink JA, van Kester JATM, Stelling GS. 2004. Development and validation of a three-dimensional morphological model. Coastal Engineering. 51(8):883-915.

Lesser GR. 2009. An approach to medium-term coastal morphological modelling. PhD thesis, UNEESCO-IHE & Delft Technical University, Delft. CRC Press/Balkema. ISBN 978-0-415-55668-2.

Mantua NJ, Hare SR, Zhang Y, Wallace JM, Francis RC. 1997. A Pacific interdecadal climate oscillation with impacts on salmon production. Bull. Amer. Meteor. Soc., 78: 1069–1079.

Molina MO, Gutiérrez C, Sánchez E. 2021. Comparison of era5 surface wind speed climatologies over Europe with observations from the HADIST dataset. International Journal of Climatology. 41(10):4864-4878.

Morim J, Hemer M, Wang XL, Cartwright N, Trenham C, Semedo A, Young I, Bricheno L, Camus P, Casas-Prat M et al. 2019. Robustness and uncertainties in global multivariate wind-wave climate projections. Nature Climate Change. 9(9):711-718.

Nederhoff K, Erikson L, Engelstad A, Bieniek P, Kasper J. 2022. The effect of changing sea ice on wave climate trends along Alaska's central Beaufort Sea coast. The Cryosphere. 16(5):1609-1629.

Nederhoff K, Erikson LH, Engelstad A, Pearson, S. Lagrangian sediment transport modeling in current and future climate along the North Slope of Alaska. Proc. Coastal Sediments '23. Wiley Publishers. 2023. 11pp.

Pearson S, Elias EPL, van Ormondt M, Roelvink FE, Lambregts PM, Wang Z, van Projjijen B. Lagrangian sediment transport modelling as a tool for investigating coastal connectivity. Coastal Dynamics Conference 2021; 2021; Delft, Netherlands.

de Queiroz, B. 2017. Input Reduction Analysis for Long-term Morphodynamic Simulations. MSc thesis, TU Delft repository. 128 pp. https:\\repository.tudelft.nl/islandora/object/uuid%3Abde676eb-2ebb-4e09-9fe9-18b5d18a246e

Raubenheimer B, Guza RT, Elgar S. 1996. Wave transformation across the inner surf zone. Journal of Geophysical Research: Oceans. 101(C11):25589-25597.

Riahi K, Rao S, Krey V, Cho C, Chirkov V, Fischer G, Kindermann G, Nakicenovic N, Rafaj P. 2011. Rcp 8.5—a scenario of comparatively high greenhouse gas emissions. Climatic Change. 109(1-2):33-57.

Scheel F. 2017. Input reduction tool - description and user manual. Deltares, Netherlands: Deltares. p. 7.

Semtner AJ. 1976. A model for the thermodynamic growth of sea ice in numerical investigations of climate. Journal of Physical Oceanography. 6(3):379-389.

Sillmann J, Kharin VV, Zhang X, Zwiers FW, Bronaugh D. 2013a. Climate extremes indices in the CMIP5 multimodel ensemble: Part 1. Model evaluation in the present climate. Journal of Geophysical Research: Atmospheres. 118(4):1716-1733.

Sillmann J, Kharin VV, Zwiers FW, Zhang X, Bronaugh D. 2013b. Climate extremes indices in the CMIP5 multimodel ensemble: Part 2. Future climate projections. Journal of Geophysical Research: Atmospheres. 118(6):2473-2493.

Stevens AW, Elias E, Pearson S, Kaminsky GM, Ruggiero PR, Weiner HM, Gelfenbaum GR. 2020. Observations of coastal change and numerical modeling of sediment-transport pathways at the mouth of the Columbia River and its adjacent littoral cell: U.S. Geological Survey Open-File Report 2020–1045, 82 p., https://doi.org//10.3133/ofr202

Stroeve JC, Crawford AD, Stammer JS. 2016. Using timing of ice retreat to predict timing of fall freeze-up in the Arctic. Geophysical Research Letters. 43(12):6332-6340.

Trefry JH, Trocine RP, Alkire MB, Semmler CM, Savoie M, Rember RD. 2009. Canimida tasks 3 and 4: Sources, concentrations, composition, partitioning and dispersal pathways for suspended sediments and potential metal contaminants in the coastal beaufort sea. Final report. Sources, concentrations, composition, partitioning and dispersion pathways for suspended sediments and potential metal contaminants in the Coastal Beaufort Sea.2009-2014.

Trefry JH, Trocine RP, Alkire MB, Woodall DW, Rember RD, Savoie M, Durell G. 2005. Sources, concentrations and dispersion pathways for suspended sediments and partitioning of potential pollutants between dissolved and particulate phases. Report 37 Alaska Minerals Management Service. (2005):37.

van der Wegen M, Jaffe BE, Roelvink JA. 2011. Process-based, morphodynamic hindcast of decadal deposition patterns in san pablo bay, california, 1856-1887. Journal of Geophysical Research: Earth Surface. 116(F2).

de Vriend HJ, Capobianco M, Chesher T, Dde Swart HE, Latteux B, Stive MJF. 1993. Approaches to long-term modelling of coastal morphology: A review. Coastal Engineering. 21:49.

Walstra DJR, Hoekstra R, Tonnon PK, Ruessink BG. 2013. Input reduction for long-term morphodynamic simulations in wave-dominated coastal settings. Coastal Engineering. 77:57-70.

Wang XL, Swail VR. 2005. Climate change signal and uncertainty in projections of ocean wave heights. Climate Dynamics. 26(2-3):109-126.

Appendix A: List of available data files produced for this study

Animations

mass_wasting_2019.avi
mass_wasting_2019_zoomin.avi
waves_with_and_without_LIB_v3.gif
qss_with_and_withoutLIB_v2.gif

Model setup

Tier1 hydrodynamic model

Stefansson Sound / Foggy Island Bay hydrodynamic model

coops_obs.xyn
cosmos_ak.fou
cosmos_ak.mdu
cosmos_ak_0000.mdu
cosmos_ak_0001.mdu
cosmos_ak_0002.mdu
cosmos_ak_0003.mdu
cosmos_ak_0004.mdu
cosmos_ak_0005.mdu
cosmos_ak_0006.mdu
cosmos_ak_0007.mdu
cosmos_ak_0008.mdu
cosmos_ak_0009.mdu
cosmos_ak_0010.mdu
cosmos_ak_0011.mdu
cosmos_ak_0012.mdu
cosmos_ak_0013.mdu
cosmos_ak_0014.mdu
cosmos_ak_0015.mdu
cosmos_ak_0016.mdu
cosmos_ak_0017.mdu
cosmos_ak_0018.mdu
cosmos_ak_0019.mdu
cosmos_ak_0020.mdu
cosmos_ak_0021.mdu
cosmos_ak_0022.mdu
cosmos_ak_0023.mdu
cosmos_ak_0024.mdu
cosmos_ak_0025.mdu
cosmos_ak_0026.mdu
cosmos_ak_0027.mdu
cosmos_ak_0028.mdu
cosmos_ak_0029.mdu
cosmos_ak_0030.mdu
cosmos_ak_0031.mdu
cosmos_ak_0032.mdu
cosmos_ak_0033.mdu
cosmos_ak_0034.mdu
cosmos_ak_0035.mdu
cosmos_ak_0036.mdu
cosmos_ak_0037.mdu
cosmos_ak_0038.mdu
cosmos_ak_0039.mdu
DFM_AKwide_outputPoints_obs.xyn
forcing_new.ext
forcing_old.ext
ISOCOLOUR.hls
ShorelineS_obs.xyn
unstruc.dia
unstruc.ini
YY1979.slurm

Tier2 coupled wave-hydrodynamic-sediment transport model

Stefansson Sound / Foggy Island Bay wave-hydrodynamic-sediment transport model, including sample input files for the 2017 open water season.

_batch_flow_wave_8cores_regular.bat	fib_detail.rgh
run_dflow2d3d_parallel.bat	fib_detail_v2.rgh
run_dflow2d3d_parallel_dwaves.bat	config_dflow2d3d.xml
fib_detail.bnd	meteo.amu
fib_detail_v2.dep	meteo.amv
swan_200m.dep	meteo.amp
fib_detail.enc	fib_detail.bcc
swan_200m.enc	fib_detail.bct
fart.exe	barrier_withLDI.pol
fib_detail.grd	barrier.pol
swan_200m.grd	fib_detail.thd
dioconfig.ini	fib_detail_withLDI.thd
fib_detail.mdf	sed_depth_clay.sdb
fib.mdw	sed_depth_pebble.sdb
fib.mor	sed_depth_sand.sdb
fib_detail.obs	sed_depth_silt.sdb
barrier.obt	fib.sed

Tier2 standalone wave model

Stefansson Sound / Foggy Island Bay standalone wave model

Batch_wave.bat
Fib.mdw
Output.loc

Sediment transport

GeoTiff files showing mapped outputs of modeled mean sediment transport potentials. Files are labeled to show the magnitude, and individual east-west ('x') and north-south ('y') component transports. Transport potentials for each of the 30 sea states listed in Table 3.1 are provided (named seastate1…. Seastate30). Mean transport fields of the entire 40-year hindcast (era5) and 30-year projections were calculated by summing individual sea state transport potentials multiplied by their probability of occurrence (Table 3.2). Note that a 31st sea state of negligible to low sediment transport potentials was used to represent under-ice conditions. Projected transports are provided for each GCM (GFDL_CMIP5, CNRM, ECEarth, and HadGemSST; see Table 2.1 for more details) and the ensemble.

Geotiff

Files in geotiff format

CNRM_transport_magnitude.tiff	seastate13_transport_magnitude.tiff
CNRM_transport_x.tiff	seastate13_transport_x.tiff

CNRM_transport_y.tiff
ECEarth_transport_magnitude.tiff
ECEarth_transport_x.tiff
ECEarth_transport_y.tiff
ensemble_transport_magnitude.tiff
ensemble_transport_x.tiff
ensemble_transport_y.tiff
era5_transport_magnitude.tiff
era5_transport_x.tiff
era5_transport_y.tiff
GFDL_CMIP5_transport_magnitude.tiff
GFDL_CMIP5_transport_x.tiff
GFDL_CMIP5_transport_y.tiff
HadGemSST_transport_magnitude.tiff
HadGemSST_transport_x.tiff
HadGemSST_transport_y.tiff
seastate01_transport_magnitude.tiff
seastate01_transport_x.tiff
seastate01_transport_y.tiff
seastate02_transport_magnitude.tiff
seastate02_transport_x.tiff
seastate02_transport_y.tiff
seastate03_transport_magnitude.tiff
seastate03_transport_x.tiff
seastate03_transport_y.tiff
seastate04_transport_magnitude.tiff
seastate04_transport_x.tiff
seastate04_transport_y.tiff
seastate05_transport_magnitude.tiff
seastate05_transport_x.tiff
seastate05_transport_y.tiff
seastate06_transport_magnitude.tiff
seastate06_transport_x.tiff
seastate06_transport_y.tiff
seastate07_transport_magnitude.tiff
seastate07_transport_x.tiff
seastate07_transport_y.tiff
seastate08_transport_magnitude.tiff
seastate08_transport_x.tiff
seastate08_transport_y.tiff
seastate09_transport_magnitude.tiff
seastate13_transport_y.tiff
seastate14_transport_magnitude.tiff
seastate14_transport_x.tiff
seastate14_transport_y.tiff
seastate15_transport_magnitude.tiff
seastate15_transport_x.tiff
seastate15_transport_y.tiff
seastate16_transport_magnitude.tiff
seastate16_transport_x.tiff
seastate16_transport_y.tiff
seastate17_transport_magnitude.tiff
seastate17_transport_x.tiff
seastate17_transport_y.tiff
seastate18_transport_magnitude.tiff
seastate18_transport_x.tiff
seastate18_transport_y.tiff
seastate19_transport_magnitude.tiff
seastate19_transport_x.tiff
seastate19_transport_y.tiff
seastate20_transport_magnitude.tiff
seastate20_transport_x.tiff
seastate20_transport_y.tiff
seastate21_transport_magnitude.tiff
seastate21_transport_x.tiff
seastate21_transport_y.tiff
seastate22_transport_magnitude.tiff
seastate22_transport_x.tiff
seastate22_transport_y.tiff
seastate23_transport_magnitude.tiff
seastate23_transport_x.tiff
seastate23_transport_y.tiff
seastate24_transport_magnitude.tiff
seastate24_transport_x.tiff
seastate24_transport_y.tiff
seastate25_transport_magnitude.tiff
seastate25_transport_x.tiff
seastate25_transport_y.tiff
seastate26_transport_magnitude.tiff
seastate26_transport_x.tiff
seastate26_transport_y.tiff
seastate27_transport_magnitude.tiff

seastate09_transport_x.tiff
seastate09_transport_y.tiff
seastate10_transport_magnitude.tiff
seastate10_transport_x.tiff
seastate10_transport_y.tiff
seastate11_transport_magnitude.tiff
seastate11_transport_x.tiff
seastate11_transport_y.tiff
seastate12_transport_magnitude.tiff
seastate12_transport_x.tiff
seastate12_transport_y.tiff
seastate27_transport_x.tiff
seastate27_transport_y.tiff
seastate28_transport_magnitude.tiff
seastate28_transport_x.tiff
seastate28_transport_y.tiff
seastate29_transport_magnitude.tiff
seastate29_transport_x.tiff
seastate29_transport_y.tiff
seastate30_transport_magnitude.tiff
seastate30_transport_x.tiff
seastate30_transport_y.tiff

netcdf

Files in netCDF format

CNRM_transport_magnitude.nc
CNRM_transport_x.nc
CNRM_transport_y.nc
ECEarth_transport_magnitude.nc
ECEarth_transport_x.nc
ECEarth_transport_y.nc
ensemble_transport_magnitude.nc
ensemble_transport_x.nc
ensemble_transport_y.nc
era5_transport_magnitude.nc
era5_transport_x.nc
era5_transport_y.nc
GFDL_CMIP5_transport_magnitude.nc
GFDL_CMIP5_transport_x.nc
GFDL_CMIP5_transport_y.nc
HadGemSST_transport_magnitude.nc
HadGemSST_transport_x.nc
HadGemSST_transport_y.nc
seastate01_transport_magnitude.nc
seastate01_transport_x.nc
seastate01_transport_y.nc
seastate02_transport_magnitude.nc
seastate02_transport_x.nc
seastate02_transport_y.nc
seastate03_transport_magnitude.nc
seastate03_transport_x.nc
seastate03_transport_y.nc
seastate04_transport_magnitude.nc
seastate04_transport_x.nc
seastate13_transport_magnitude.nc
seastate13_transport_x.nc
seastate13_transport_y.nc
seastate14_transport_magnitude.nc
seastate14_transport_x.nc
seastate14_transport_y.nc
seastate15_transport_magnitude.nc
seastate15_transport_x.nc
seastate15_transport_y.nc
seastate16_transport_magnitude.nc
seastate16_transport_x.nc
seastate16_transport_y.nc
seastate17_transport_magnitude.nc
seastate17_transport_x.nc
seastate17_transport_y.nc
seastate18_transport_magnitude.nc
seastate18_transport_x.nc
seastate18_transport_y.nc
seastate19_transport_magnitude.nc
seastate19_transport_x.nc
seastate19_transport_y.nc
seastate20_transport_magnitude.nc
seastate20_transport_x.nc
seastate20_transport_y.nc
seastate21_transport_magnitude.nc
seastate21_transport_x.nc
seastate21_transport_y.nc
seastate22_transport_magnitude.nc
seastate22_transport_x.nc

seastate04_transport_y.nc
seastate05_transport_magnitude.nc
seastate05_transport_x.nc
seastate05_transport_y.nc
seastate06_transport_magnitude.nc
seastate06_transport_x.nc
seastate06_transport_y.nc
seastate07_transport_magnitude.nc
seastate07_transport_x.nc
seastate07_transport_y.nc
seastate08_transport_magnitude.nc
seastate08_transport_x.nc
seastate08_transport_y.nc
seastate09_transport_magnitude.nc
seastate09_transport_x.nc
seastate09_transport_y.nc
seastate10_transport_magnitude.nc
seastate10_transport_x.nc
seastate10_transport_y.nc
seastate11_transport_magnitude.nc
seastate11_transport_x.nc
seastate11_transport_y.nc
seastate12_transport_magnitude.nc
seastate12_transport_x.nc
seastate12_transport_y.nc
seastate22_transport_y.nc
seastate23_transport_magnitude.nc
seastate23_transport_x.nc
seastate23_transport_y.nc
seastate24_transport_magnitude.nc
seastate24_transport_x.nc
seastate24_transport_y.nc
seastate25_transport_magnitude.nc
seastate25_transport_x.nc
seastate25_transport_y.nc
seastate26_transport_magnitude.nc
seastate26_transport_x.nc
seastate26_transport_y.nc
seastate27_transport_magnitude.nc
seastate27_transport_x.nc
seastate27_transport_y.nc
seastate28_transport_magnitude.nc
seastate28_transport_x.nc
seastate28_transport_y.nc
seastate29_transport_magnitude.nc
seastate29_transport_x.nc
seastate29_transport_y.nc
seastate30_transport_magnitude.nc
seastate30_transport_x.nc
seastate30_transport_y.nc

Wave return periods (Tier2A)

Return period statistics from stand-alone Tier2A wave model.

Hindcast_ERA5

ERA5_Hs_Rp1.tif
ERA5_Hs_Rp10.tif
ERA5_Hs_Rp2.tif
ERA5_Hs_Rp20.tif
ERA5_Hs_Rp30.tif
ERA5_Hs_Rp5.tif

Projected_CMIP5_GFDL

cmip5_gfdl_Hs_Rp1.tif
cmip5_gfdl_Hs_Rp10.tif
cmip5_gfdl_Hs_Rp2.tif
cmip5_gfdl_Hs_Rp20.tif
cmip5_gfdl_Hs_Rp30.tif
cmip5_gfdl_Hs_Rp5.tif

Wave return periods (Tier2B DWDB)

Hindcast_ERA5

Return period statistics for the hindcast period 1979-2019.

ERA5_Hs_Rp1.tif
ERA5_Hs_Rp10.tif
ERA5_Hs_Rp2.tif
ERA5_Hs_Rp20.tif
ERA5_Hs_Rp30.tif
ERA5_Hs_Rp5.tif

Projected_CMIP5_GFDL

Return period statistics for the projected period 2020-2050.

cmip5_gfdl_Hs_Rp1.tif
cmip5_gfdl_Hs_Rp10.tif
cmip5_gfdl_Hs_Rp2.tif
cmip5_gfdl_Hs_Rp20.tif
cmip5_gfdl_Hs_Rp30.tif
cmip5_gfdl_Hs_Rp5.tif

Projected_CMIP6

Return period statistics for the projected period 2020-2050.

CMCC_Hs_Rp1.tif	HadGEM_HH_Hs_Rp1.tif
CMCC_Hs_Rp10.tif	HadGEM_HH_Hs_Rp10.tif
CMCC_Hs_Rp2.tif	HadGEM_HH_Hs_Rp2.tif
CMCC_Hs_Rp20.tif	HadGEM_HH_Hs_Rp20.tif
CMCC_Hs_Rp30.tif	HadGEM_HH_Hs_Rp30.tif
CMCC_Hs_Rp5.tif	HadGEM_HH_Hs_Rp5.tif
CNRM_Hs_Rp1.tif	HadGEM_HM_Hs_Rp1.tif
CNRM_Hs_Rp10.tif	HadGEM_HM_Hs_Rp10.tif
CNRM_Hs_Rp2.tif	HadGEM_HM_Hs_Rp2.tif
CNRM_Hs_Rp20.tif	HadGEM_HM_Hs_Rp20.tif
CNRM_Hs_Rp30.tif	HadGEM_HM_Hs_Rp30.tif
CNRM_Hs_Rp5.tif	HadGEM_HM_Hs_Rp5.tif
EC_Earth_Hs_Rp1.tif	Hadgem_SST_Hs_Rp1.tif
EC_Earth_Hs_Rp10.tif	Hadgem_SST_Hs_Rp10.tif
EC_Earth_Hs_Rp2.tif	Hadgem_SST_Hs_Rp2.tif
EC_Earth_Hs_Rp20.tif	Hadgem_SST_Hs_Rp20.tif
EC_Earth_Hs_Rp30.tif	Hadgem_SST_Hs_Rp30.tif

EC_Earth_Hs_Rp5.tif Hadgem_SST_Hs_Rp5.tif

Wave summary statistics (Tier2A)

Hindcast_ERA5

Hindcast DWDB wave standalone model results.

GeoTiff files showing mapped outputs of modeled wave height (Hs), mean wave period (Tm), wave directions (Dm), wave steepness, orbital velocity, wind speed, sea ice concentrations, and wave power summary statistics from 3-hourly model outputs between 1979–2019. Results are from model 'Tier2A intermediate' wave model grid. File names with 0.250, 0.500, etc., refer to the percentiles over the 40-year hindcast. Tier2A model results consider all time steps (including times of ice cover).

Hs_0.750_utm.tif	steepness_0.250.tiff
Hs_0.950_utm.tif	steepness_0.500.tiff
Hs_0.995_utm.tif	steepness_0.750.tiff
Hs_max_utm.tif	steepness_0.950.tiff
Hs_mean_utm.tif	steepness_0.995.tiff
Dm_0.250.tiff	steepness_max.tiff
Dm_0.500.tiff	steepness_mean.tiff
Dm_0.750.tiff	steepness_min.tiff
Dm_0.950.tiff	Tm_0.250.tiff
Dm_0.995.tiff	Tm_0.500.tiff
Dm_max.tiff	Tm_0.750.tiff
Dm_mean.tiff	Tm_0.950.tiff
Dm_min.tiff	Tm_0.995.tiff
Hs_0.250.tiff	Tm_max.tiff
Hs_0.500.tiff	Tm_mean.tiff
Hs_0.750.tiff	Tm_min.tiff
Hs_0.950.tiff	umag_0.250.tiff
Hs_0.995.tiff	umag_0.500.tiff
Hs_max.tiff	umag_0.750.tiff
Hs_mean.tiff	umag_0.950.tiff
Hs_min.tiff	umag_0.995.tiff
ice_0.250.tiff	umag_max.tiff
ice_0.500.tiff	umag_mean.tiff
ice_0.750.tiff	umag_min.tiff
ice_0.950.tiff	wave_power_0.250.tiff
ice_0.995.tiff	wave_power_0.500.tiff
ice_max.tiff	wave_power_0.750.tiff
ice_mean.tiff	wave_power_0.950.tiff
ice_min.tiff	wave_power_0.995.tiff
orbital_0.250.tiff	wave_power_max.tiff
orbital_0.500.tiff	wave_power_mean.tiff

orbital_0.750.tiff
orbital_0.950.tiff
orbital_0.995.tiff
orbital_max.tiff
orbital_mean.tiff
orbital_min.tiff
wave_power_min.tiff

Projected_CMIP5_GFDL

CMIP5projected wave standalone model results

GeoTiff files showing mapped outputs of modeled wave height (Hs), mean wave period (Tm), wave directions (Dm), wave steepness, orbital velocity, wind speeds, sea ice concentrations, and wave power summary statistics from 3-hourly model outputs between 2020–2050. Results are from model 'Tier2A intermediate' wave model grid. File names with 0.250, 0.500, etc., refer to the percentiles over the 30-year projection time period. Tier2A model results consider all time steps (including times of ice coverage).

Hs_0.750_utm.tif
Hs_0.950_utm.tif
Hs_0.995_utm.tif
Hs_max_utm.tif
Hs_mean_utm.tif
Dm_0.250.tiff
Dm_0.500.tiff
Dm_0.750.tiff
Dm_0.950.tiff
Dm_0.995.tiff
Dm_max.tiff
Dm_mean.tiff
Dm_min.tiff
Hs_0.250.tiff
Hs_0.500.tiff
Hs_0.750.tiff
Hs_0.950.tiff
Hs_0.995.tiff
Hs_max.tiff
Hs_mean.tiff
Hs_min.tiff
ice_0.250.tiff
ice_0.500.tiff
ice_0.750.tiff
ice_0.950.tiff
ice_0.995.tiff
ice_max.tiff
ice_mean.tiff
steepness_0.250.tiff
steepness_0.500.tiff
steepness_0.750.tiff
steepness_0.950.tiff
steepness_0.995.tiff
steepness_max.tiff
steepness_mean.tiff
steepness_min.tiff
Tm_0.250.tiff
Tm_0.500.tiff
Tm_0.750.tiff
Tm_0.950.tiff
Tm_0.995.tiff
Tm_max.tiff
Tm_mean.tiff
Tm_min.tiff
umag_0.250.tiff
umag_0.500.tiff
umag_0.750.tiff
umag_0.950.tiff
umag_0.995.tiff
umag_max.tiff
umag_mean.tiff
umag_min.tiff
wave_power_0.250.tiff
wave_power_0.500.tiff
wave_power_0.750.tiff
wave_power_0.950.tiff

ice_min.tiff
orbital_0.250.tiff
orbital_0.500.tiff
orbital_0.750.tiff
orbital_0.950.tiff
orbital_0.995.tiff
orbital_max.tiff
orbital_mean.tiff
orbital_min.tiff
wave_power_0.995.tiff
wave_power_max.tiff
wave_power_mean.tiff
wave_power_min.tiff

Wave summary statistics (Tier2B DWDB)

Hindcast_ERA5

Hindcast DWDB wave standalone model results.

GeoTiff files showing mapped outputs of modeled wave height (Hs), mean wave period (Tm), wave directions (Dm), wave steepness, orbital velocity, depth-averaged currents, sea ice concentrations, and wave power summary statistics from 3-hourly model outputs between 1979–2019. Results are from the 'Tier2B' wave model. File names with 0.250, 0.500, etc., and RP1, RP2, etc., refer to the percentiles and return period values over the 40-year hindcast, respectively.

TimesLowIce

Summary statistics, excluding time-points when sea ice concentrations >15%

ERA5_Dm_0.250.tif
ERA5_Dm_0.500.tif
ERA5_Dm_0.750.tif
ERA5_Dm_0.9.tif
ERA5_Dm_0.950.tif
ERA5_Dm_0.995.tif
ERA5_Dm_max.tif
ERA5_Dm_mean.tif
ERA5_Hs_0.250.tif
ERA5_Hs_0.500.tif
ERA5_Hs_0.750.tif
ERA5_Hs_0.9.tif
ERA5_Hs_0.950.tif
ERA5_Hs_0.995.tif
ERA5_Hs_max.tif
ERA5_Hs_mean.tif
ERA5_orbital_0.250.tif
ERA5_orbital_0.500.tif
ERA5_orbital_0.750.tif
ERA5_steepness_0.250.tif
ERA5_steepness_0.500.tif
ERA5_steepness_0.750.tif
ERA5_steepness_0.9.tif
ERA5_steepness_0.950.tif
ERA5_steepness_0.995.tif
ERA5_steepness_max.tif
ERA5_steepness_mean.tif
ERA5_Tm_0.250.tif
ERA5_Tm_0.500.tif
ERA5_Tm_0.750.tif
ERA5_Tm_0.9.tif
ERA5_Tm_0.950.tif
ERA5_Tm_0.995.tif
ERA5_Tm_max.tif
ERA5_Tm_mean.tif
ERA5_wave_power_0.250.tif
ERA5_wave_power_0.500.tif
ERA5_wave_power_0.750.tif

ERA5_orbital_0.9.tif	ERA5_wave_power_0.9.tif
ERA5_orbital_0.950.tif	ERA5_wave_power_0.950.tif
ERA5_orbital_0.995.tif	ERA5_wave_power_0.995.tif
ERA5_orbital_max.tif	ERA5_wave_power_max.tif
ERA5_orbital_mean.tif	ERA5_wave_power_mean.tif

AllTimePoints

Summary statistics, including all time-points, including full ice cover. These are only available for wave heights and wave power since all other variables were set to "Not a Number" (NaN) for wave heights < 0.15 m to avoid spurious results.

ERA5_Hs_0.250.tif
ERA5_Hs_0.500.tif
ERA5_Hs_0.750.tif
ERA5_Hs_0.9.tif
ERA5_Hs_0.950.tif
ERA5_Hs_0.995.tif
ERA5_Hs_max.tif
ERA5_Hs_mean.tif
ERA5_wave_power_0.250.tif
ERA5_wave_power_0.500.tif
ERA5_wave_power_0.750.tif
ERA5_wave_power_0.9.tif
ERA5_wave_power_0.950.tif
ERA5_wave_power_0.995.tif
ERA5_wave_power_max.tif
ERA5_wave_power_mean.tif

Projected_CMIP5_GFDL

CMIP5 projected DWDB wave standalone model results

GeoTiff files showing mapped outputs of modeled wave height (Hs), mean wave period (Tm), wave directions (Dm), wave steepness, orbital velocity, depth-averaged currents, sea ice concentrations, and wave power summary statistics from 3-hourly model outputs between 2020–2050. Results from the CMIP5 GFDL-CM3 GCM are provided. See Table 2.1 for more details. Model results are from the 'Tier2B' wave model. File names with 0.250, 0.500, etc., and RP1, RP2, etc., refer to the percentiles and return period values, over the 30-year projection time period.

TimesLowIce

Summary statistics, excluding time-points when sea ice concentrations >15%

CMIP5_GFDL_Dm_0.250.tif	CMIP5_GFDL_steepness_0.250.tif
CMIP5_GFDL_Dm_0.500.tif	CMIP5_GFDL_steepness_0.500.tif
CMIP5_GFDL_Dm_0.750.tif	CMIP5_GFDL_steepness_0.750.tif
CMIP5_GFDL_Dm_0.9.tif	CMIP5_GFDL_steepness_0.9.tif
CMIP5_GFDL_Dm_0.950.tif	CMIP5_GFDL_steepness_0.950.tif

CMIP5_GFDL_Dm_0.995.tif	CMIP5_GFDL_steepness_0.995.tif
CMIP5_GFDL_Dm_max.tif	CMIP5_GFDL_steepness_max.tif
CMIP5_GFDL_Dm_mean.tif	CMIP5_GFDL_steepness_mean.tif
CMIP5_GFDL_Hs_0.250.tif	CMIP5_GFDL_Tm01_0.250.tif
CMIP5_GFDL_Hs_0.500.tif	CMIP5_GFDL_Tm01_0.500.tif
CMIP5_GFDL_Hs_0.750.tif	CMIP5_GFDL_Tm01_0.750.tif
CMIP5_GFDL_Hs_0.9.tif	CMIP5_GFDL_Tm01_0.9.tif
CMIP5_GFDL_Hs_0.950.tif	CMIP5_GFDL_Tm01_0.950.tif
CMIP5_GFDL_Hs_0.995.tif	CMIP5_GFDL_Tm01_0.995.tif
CMIP5_GFDL_Hs_max.tif	CMIP5_GFDL_Tm01_max.tif
CMIP5_GFDL_Hs_mean.tif	CMIP5_GFDL_Tm01_mean.tif
CMIP5_GFDL_orbital_0.250.tif	CMIP5_GFDL_wave_power_0.250.tif
CMIP5_GFDL_orbital_0.500.tif	CMIP5_GFDL_wave_power_0.500.tif
CMIP5_GFDL_orbital_0.750.tif	CMIP5_GFDL_wave_power_0.750.tif
CMIP5_GFDL_orbital_0.9.tif	CMIP5_GFDL_wave_power_0.9.tif
CMIP5_GFDL_orbital_0.950.tif	CMIP5_GFDL_wave_power_0.950.tif
CMIP5_GFDL_orbital_0.995.tif	CMIP5_GFDL_wave_power_0.995.tif
CMIP5_GFDL_orbital_max.tif	CMIP5_GFDL_wave_power_max.tif
CMIP5_GFDL_orbital_mean.tif	CMIP5_GFDL_wave_power_mean.tif

AllTimePoints

These are only available for wave heights and wave power since all other variables were set to "Not a Number" (NaN) for wave heights < 0.15 m to avoid spurious results.

CMIP5_GFDL_Hs_0.250.tif
CMIP5_GFDL_Hs_0.500.tif
CMIP5_GFDL_Hs_0.750.tif
CMIP5_GFDL_Hs_0.9.tif
CMIP5_GFDL_Hs_0.950.tif
CMIP5_GFDL_Hs_0.995.tif
CMIP5_GFDL_Hs_max.tif
CMIP5_GFDL_Hs_mean.tif
CMIP5_GFDL_wave_power_0.250.tif
CMIP5_GFDL_wave_power_0.500.tif
CMIP5_GFDL_wave_power_0.750.tif
CMIP5_GFDL_wave_power_0.9.tif
CMIP5_GFDL_wave_power_0.950.tif
CMIP5_GFDL_wave_power_0.995.tif
CMIP5_GFDL_wave_power_max.tif
CMIP5_GFDL_wave_power_mean.tif

Projected_CMIP6

CMIP6 projected DWDB wave standalone model results.

GeoTiff files showing mapped outputs of modeled wave height (Hs), mean wave period (Tm), wave directions (Dm), wave steepness, orbital velocity, depth-averaged currents, sea ice concentrations, and wave power summary statistics from 3-hourly model outputs between 2020–2050. Results from each individual CMIP6 GCM and ensemble mean are provided. See Table 2.1 for a list and details on the GCMs. Results are from the 'Tier2B' wave model. File names with 0.250, 0.500, etc., and RP1, RP2, etc., refer to the percentiles and return period values, over the 30-year projection time period.

TimesLowIce

Summary statistics of individual GCMs, excluding time-points when sea ice concentrations >15%.

CMCC_Dm_0.250.tif
CMCC_Dm_0.500.tif
CMCC_Dm_0.750.tif
CMCC_Dm_0.9.tif
CMCC_Dm_0.950.tif
CMCC_Dm_0.995.tif
CMCC_Dm_max.tif
CMCC_Dm_mean.tif
CMCC_Hs_0.250.tif
CMCC_Hs_0.500.tif
CMCC_Hs_0.750.tif
CMCC_Hs_0.9.tif
CMCC_Hs_0.950.tif
CMCC_Hs_0.995.tif
CMCC_Hs_max.tif
CMCC_Hs_mean.tif
CMCC_orbital_0.250.tif
CMCC_orbital_0.500.tif
CMCC_orbital_0.750.tif
CMCC_orbital_0.9.tif
CMCC_orbital_0.950.tif
CMCC_orbital_0.995.tif
CMCC_orbital_max.tif
CMCC_orbital_mean.tif
CMCC_steepness_0.250.tif
CMCC_steepness_0.500.tif
CMCC_steepness_0.750.tif
CMCC_steepness_0.9.tif
CMCC_steepness_0.950.tif
CMCC_steepness_0.995.tif
CMCC_steepness_max.tif
CMCC_steepness_mean.tif
CMCC_Tm01_0.250.tif
EC_Earth_Dm_0.950.tif
EC_Earth_Dm_0.995.tif
EC_Earth_Dm_max.tif
EC_Earth_Dm_mean.tif
EC_Earth_Hs_0.250.tif
EC_Earth_Hs_0.500.tif
EC_Earth_Hs_0.750.tif
EC_Earth_Hs_0.9.tif
EC_Earth_Hs_0.950.tif
EC_Earth_Hs_0.995.tif
EC_Earth_Hs_max.tif
EC_Earth_Hs_mean.tif
EC_Earth_orbital_0.250.tif
EC_Earth_orbital_0.500.tif
EC_Earth_orbital_0.750.tif
EC_Earth_orbital_0.9.tif
EC_Earth_orbital_0.950.tif
EC_Earth_orbital_0.995.tif
EC_Earth_orbital_max.tif
EC_Earth_orbital_mean.tif
EC_Earth_steepness_0.250.tif
EC_Earth_steepness_0.500.tif
EC_Earth_steepness_0.750.tif
EC_Earth_steepness_0.9.tif
EC_Earth_steepness_0.950.tif
EC_Earth_steepness_0.995.tif
EC_Earth_steepness_max.tif
EC_Earth_steepness_mean.tif
EC_Earth_Tm01_0.250.tif
EC_Earth_Tm01_0.500.tif
EC_Earth_Tm01_0.750.tif
EC_Earth_Tm01_0.9.tif
EC_Earth_Tm01_0.950.tif
HadGEM_HM_Hs_0.250.tif
HadGEM_HM_Hs_0.500.tif
HadGEM_HM_Hs_0.750.tif
HadGEM_HM_Hs_0.9.tif
HadGEM_HM_Hs_0.950.tif
HadGEM_HM_Hs_0.995.tif
HadGEM_HM_Hs_max.tif
HadGEM_HM_Hs_mean.tif
HadGEM_HM_orbital_0.250.tif
HadGEM_HM_orbital_0.500.tif
HadGEM_HM_orbital_0.750.tif
HadGEM_HM_orbital_0.9.tif
HadGEM_HM_orbital_0.950.tif
HadGEM_HM_orbital_0.995.tif
HadGEM_HM_orbital_max.tif
HadGEM_HM_orbital_mean.tif
HadGEM_HM_steepness_0.250.tif
HadGEM_HM_steepness_0.500.tif
HadGEM_HM_steepness_0.750.tif
HadGEM_HM_steepness_0.9.tif
HadGEM_HM_steepness_0.950.tif
HadGEM_HM_steepness_0.995.tif
HadGEM_HM_steepness_max.tif
HadGEM_HM_steepness_mean.tif
HadGEM_HM_Tm01_0.250.tif
HadGEM_HM_Tm01_0.500.tif
HadGEM_HM_Tm01_0.750.tif
HadGEM_HM_Tm01_0.9.tif
HadGEM_HM_Tm01_0.950.tif
HadGEM_HM_Tm01_0.995.tif
HadGEM_HM_Tm01_max.tif
HadGEM_HM_Tm01_mean.tif
HadGEM_HM_wave_power_0.250.tif

CMCC_Tm01_0.500.tif
CMCC_Tm01_0.750.tif
CMCC_Tm01_0.9.tif
CMCC_Tm01_0.950.tif
CMCC_Tm01_0.995.tif
CMCC_Tm01_max.tif
CMCC_Tm01_mean.tif
CMCC_wave_power_0.250.tif
CMCC_wave_power_0.500.tif
CMCC_wave_power_0.750.tif
CMCC_wave_power_0.9.tif
CMCC_wave_power_0.950.tif
CMCC_wave_power_0.995.tif
CMCC_wave_power_max.tif
CMCC_wave_power_mean.tif
CNRM_Dm_0.250.tif
CNRM_Dm_0.500.tif
CNRM_Dm_0.750.tif
CNRM_Dm_0.9.tif
CNRM_Dm_0.950.tif
CNRM_Dm_0.995.tif
CNRM_Dm_max.tif
CNRM_Dm_mean.tif
CNRM_Hs_0.250.tif
CNRM_Hs_0.500.tif
CNRM_Hs_0.750.tif
CNRM_Hs_0.9.tif
CNRM_Hs_0.950.tif
CNRM_Hs_0.995.tif
CNRM_Hs_max.tif
CNRM_Hs_mean.tif
CNRM_orbital_0.250.tif
CNRM_orbital_0.500.tif
CNRM_orbital_0.750.tif
CNRM_orbital_0.9.tif
CNRM_orbital_0.950.tif
CNRM_orbital_0.995.tif
CNRM_orbital_max.tif
CNRM_orbital_mean.tif
CNRM_steepness_0.250.tif
CNRM_steepness_0.500.tif
CNRM_steepness_0.750.tif
CNRM_steepness_0.9.tif
EC_Earth_Tm01_0.995.tif
EC_Earth_Tm01_max.tif
EC_Earth_Tm01_mean.tif
EC_Earth_wave_power_0.250.tif
EC_Earth_wave_power_0.500.tif
EC_Earth_wave_power_0.750.tif
EC_Earth_wave_power_0.9.tif
EC_Earth_wave_power_0.950.tif
EC_Earth_wave_power_0.995.tif
EC_Earth_wave_power_max.tif
EC_Earth_wave_power_mean.tif
HadGEM_HH_Dm_0.250.tif
HadGEM_HH_Dm_0.500.tif
HadGEM_HH_Dm_0.750.tif
HadGEM_HH_Dm_0.9.tif
HadGEM_HH_Dm_0.950.tif
HadGEM_HH_Dm_0.995.tif
HadGEM_HH_Dm_max.tif
HadGEM_HH_Dm_mean.tif
HadGEM_HH_Hs_0.250.tif
HadGEM_HH_Hs_0.500.tif
HadGEM_HH_Hs_0.750.tif
HadGEM_HH_Hs_0.9.tif
HadGEM_HH_Hs_0.950.tif
HadGEM_HH_Hs_0.995.tif
HadGEM_HH_Hs_max.tif
HadGEM_HH_Hs_mean.tif
HadGEM_HH_orbital_0.250.tif
HadGEM_HH_orbital_0.500.tif
HadGEM_HH_orbital_0.750.tif
HadGEM_HH_orbital_0.9.tif
HadGEM_HH_orbital_0.950.tif
HadGEM_HH_orbital_0.995.tif
HadGEM_HH_orbital_max.tif
HadGEM_HH_orbital_mean.tif
HadGEM_HH_steepness_0.250.tif
HadGEM_HH_steepness_0.500.tif
HadGEM_HH_steepness_0.750.tif
HadGEM_HH_steepness_0.9.tif
HadGEM_HH_steepness_0.950.tif
HadGEM_HH_steepness_0.995.tif
HadGEM_HH_steepness_max.tif
HadGEM_HH_steepness_mean.tif
HadGEM_HM_wave_power_0.500.tif
HadGEM_HM_wave_power_0.750.tif
HadGEM_HM_wave_power_0.9.tif
HadGEM_HM_wave_power_0.950.tif
HadGEM_HM_wave_power_0.995.tif
HadGEM_HM_wave_power_max.tif
HadGEM_HM_wave_power_mean.tif
Hadgem_SST_Dm_0.250.tif
Hadgem_SST_Dm_0.500.tif
Hadgem_SST_Dm_0.750.tif
Hadgem_SST_Dm_0.9.tif
Hadgem_SST_Dm_0.950.tif
Hadgem_SST_Dm_0.995.tif
Hadgem_SST_Dm_max.tif
Hadgem_SST_Dm_mean.tif
Hadgem_SST_Hs_0.250.tif
Hadgem_SST_Hs_0.500.tif
Hadgem_SST_Hs_0.750.tif
Hadgem_SST_Hs_0.9.tif
Hadgem_SST_Hs_0.950.tif
Hadgem_SST_Hs_0.995.tif
Hadgem_SST_Hs_max.tif
Hadgem_SST_Hs_mean.tif
Hadgem_SST_orbital_0.250.tif
Hadgem_SST_orbital_0.500.tif
Hadgem_SST_orbital_0.750.tif
Hadgem_SST_orbital_0.9.tif
Hadgem_SST_orbital_0.950.tif
Hadgem_SST_orbital_0.995.tif
Hadgem_SST_orbital_max.tif
Hadgem_SST_orbital_mean.tif
Hadgem_SST_steepness_0.250.tif
Hadgem_SST_steepness_0.500.tif
Hadgem_SST_steepness_0.750.tif
Hadgem_SST_steepness_0.9.tif
Hadgem_SST_steepness_0.950.tif
Hadgem_SST_steepness_0.995.tif
Hadgem_SST_steepness_max.tif
Hadgem_SST_steepness_mean.tif
Hadgem_SST_Tm01_0.250.tif
Hadgem_SST_Tm01_0.500.tif
Hadgem_SST_Tm01_0.750.tif
Hadgem_SST_Tm01_0.9.tif

CNRM_steepness_0.950.tif
CNRM_steepness_0.995.tif
CNRM_steepness_max.tif
CNRM_steepness_mean.tif
CNRM_Tm01_0.250.tif
CNRM_Tm01_0.500.tif
CNRM_Tm01_0.750.tif
CNRM_Tm01_0.9.tif
CNRM_Tm01_0.950.tif
CNRM_Tm01_0.995.tif
CNRM_Tm01_max.tif
CNRM_Tm01_mean.tif
CNRM_wave_power_0.250.tif
CNRM_wave_power_0.500.tif
CNRM_wave_power_0.750.tif
CNRM_wave_power_0.9.tif
CNRM_wave_power_0.950.tif
CNRM_wave_power_0.995.tif
CNRM_wave_power_max.tif
CNRM_wave_power_mean.tif
EC_Earth_Dm_0.250.tif
EC_Earth_Dm_0.500.tif
EC_Earth_Dm_0.750.tif
EC_Earth_Dm_0.9.tif
HadGEM_HH_Tm01_0.250.tif
HadGEM_HH_Tm01_0.500.tif
HadGEM_HH_Tm01_0.750.tif
HadGEM_HH_Tm01_0.9.tif
HadGEM_HH_Tm01_0.950.tif
HadGEM_HH_Tm01_0.995.tif
HadGEM_HH_Tm01_max.tif
HadGEM_HH_Tm01_mean.tif
HadGEM_HH_wave_power_0.250.tif
HadGEM_HH_wave_power_0.500.tif
HadGEM_HH_wave_power_0.750.tif
HadGEM_HH_wave_power_0.9.tif
HadGEM_HH_wave_power_0.950.tif
HadGEM_HH_wave_power_0.995.tif
HadGEM_HH_wave_power_max.tif
HadGEM_HH_wave_power_mean.tif
HadGEM_HM_Dm_0.250.tif
HadGEM_HM_Dm_0.500.tif
HadGEM_HM_Dm_0.750.tif
HadGEM_HM_Dm_0.9.tif
HadGEM_HM_Dm_0.950.tif
HadGEM_HM_Dm_0.995.tif
HadGEM_HM_Dm_max.tif
HadGEM_HM_Dm_mean.tif
Hadgem_SST_Tm01_0.950.tif
Hadgem_SST_Tm01_0.995.tif
Hadgem_SST_Tm01_max.tif
Hadgem_SST_Tm01_mean.tif
Hadgem_SST_wave_power_0.250.tif
Hadgem_SST_wave_power_0.500.tif
Hadgem_SST_wave_power_0.750.tif
Hadgem_SST_wave_power_0.9.tif
Hadgem_SST_wave_power_0.950.tif
Hadgem_SST_wave_power_0.995.tif
Hadgem_SST_wave_power_max.tif
Hadgem_SST_wave_power_mean.tif

AllTimePoints

These are only available for wave heights and wave power since all other variables were set to "Not a Number" (NaN) for wave heights < 0.15 m to avoid spurious results.

CMCC_Hs_0.250.tif
CMCC_Hs_0.500.tif
CMCC_Hs_0.750.tif
CMCC_Hs_0.9.tif
CMCC_Hs_0.950.tif
CMCC_Hs_0.995.tif
CMCC_Hs_max.tif
CMCC_Hs_mean.tif
CMCC_wave_power_0.250.tif
CMCC_wave_power_0.500.tif
CMCC_wave_power_0.750.tif
CMCC_wave_power_0.9.tif
CMCC_wave_power_0.950.tif
CMCC_wave_power_0.995.tif
HadGEM_HH_Hs_0.250.tif
HadGEM_HH_Hs_0.500.tif
HadGEM_HH_Hs_0.750.tif
HadGEM_HH_Hs_0.9.tif
HadGEM_HH_Hs_0.950.tif
HadGEM_HH_Hs_0.995.tif
HadGEM_HH_Hs_max.tif
HadGEM_HH_Hs_mean.tif
HadGEM_HH_wave_power_0.250.tif
HadGEM_HH_wave_power_0.500.tif
HadGEM_HH_wave_power_0.750.tif
HadGEM_HH_wave_power_0.9.tif
HadGEM_HH_wave_power_0.950.tif
HadGEM_HH_wave_power_0.995.tif

CMCC_wave_power_max.tif	HadGEM_HH_wave_power_max.tif
CMCC_wave_power_mean.tif	HadGEM_HH_wave_power_mean.tif
CNRM_Hs_0.250.tif	HadGEM_HM_Hs_0.250.tif
CNRM_Hs_0.500.tif	HadGEM_HM_Hs_0.500.tif
CNRM_Hs_0.750.tif	HadGEM_HM_Hs_0.750.tif
CNRM_Hs_0.9.tif	HadGEM_HM_Hs_0.9.tif
CNRM_Hs_0.950.tif	HadGEM_HM_Hs_0.950.tif
CNRM_Hs_0.995.tif	HadGEM_HM_Hs_0.995.tif
CNRM_Hs_max.tif	HadGEM_HM_Hs_max.tif
CNRM_Hs_mean.tif	HadGEM_HM_Hs_mean.tif
CNRM_wave_power_0.250.tif	HadGEM_HM_wave_power_0.250.tif
CNRM_wave_power_0.500.tif	HadGEM_HM_wave_power_0.500.tif
CNRM_wave_power_0.750.tif	HadGEM_HM_wave_power_0.750.tif
CNRM_wave_power_0.9.tif	HadGEM_HM_wave_power_0.9.tif
CNRM_wave_power_0.950.tif	HadGEM_HM_wave_power_0.950.tif
CNRM_wave_power_0.995.tif	HadGEM_HM_wave_power_0.995.tif
CNRM_wave_power_max.tif	HadGEM_HM_wave_power_max.tif
CNRM_wave_power_mean.tif	HadGEM_HM_wave_power_mean.tif
EC_Earth_Hs_0.250.tif	Hadgem_SST_Hs_0.250.tif
EC_Earth_Hs_0.500.tif	Hadgem_SST_Hs_0.500.tif
EC_Earth_Hs_0.750.tif	Hadgem_SST_Hs_0.750.tif
EC_Earth_Hs_0.9.tif	Hadgem_SST_Hs_0.9.tif
EC_Earth_Hs_0.950.tif	Hadgem_SST_Hs_0.950.tif
EC_Earth_Hs_0.995.tif	Hadgem_SST_Hs_0.995.tif
EC_Earth_Hs_max.tif	Hadgem_SST_Hs_max.tif
EC_Earth_Hs_mean.tif	Hadgem_SST_Hs_mean.tif
EC_Earth_wave_power_0.250.tif	Hadgem_SST_wave_power_0.250.tif
EC_Earth_wave_power_0.500.tif	Hadgem_SST_wave_power_0.500.tif
EC_Earth_wave_power_0.750.tif	Hadgem_SST_wave_power_0.750.tif
EC_Earth_wave_power_0.9.tif	Hadgem_SST_wave_power_0.9.tif
EC_Earth_wave_power_0.950.tif	Hadgem_SST_wave_power_0.950.tif
EC_Earth_wave_power_0.995.tif	Hadgem_SST_wave_power_0.995.tif
EC_Earth_wave_power_max.tif	Hadgem_SST_wave_power_max.tif
EC_Earth_wave_power_mean.tif	Hadgem_SST_wave_power_mean.tif

Ensemble_TimesLowIce

Ensemble summary statistics of the five GCMs listed in Table 2.1 (i.e., mean values of individual summary statistic results). Computed statistics exclude time-points when sea ice concentrations >15%.

Ensemble_Dm_0.250.tif	Ensemble_steepness_0.250.tif
Ensemble_Dm_0.500.tif	Ensemble_steepness_0.500.tif
Ensemble_Dm_0.750.tif	Ensemble_steepness_0.750.tif
Ensemble_Dm_0.9.tif	Ensemble_steepness_0.9.tif
Ensemble_Dm_0.950.tif	Ensemble_steepness_0.950.tif

Ensemble_Dm_0.995.tif	Ensemble_steepness_0.995.tif
Ensemble_Dm_max.tif	Ensemble_steepness_max.tif
Ensemble_Dm_mean.tif	Ensemble_steepness_mean.tif
Ensemble_Hs_0.250.tif	Ensemble_Tm_0.250.tif
Ensemble_Hs_0.500.tif	Ensemble_Tm_0.500.tif
Ensemble_Hs_0.750.tif	Ensemble_Tm_0.750.tif
Ensemble_Hs_0.9.tif	Ensemble_Tm_0.9.tif
Ensemble_Hs_0.950.tif	Ensemble_Tm_0.950.tif
Ensemble_Hs_0.995.tif	Ensemble_Tm_0.995.tif
Ensemble_Hs_max.tif	Ensemble_Tm_max.tif
Ensemble_Hs_mean.tif	Ensemble_Tm_mean.tif
Ensemble_orbital_0.250.tif	Ensemble_wave_power_0.250.tif
Ensemble_orbital_0.500.tif	Ensemble_wave_power_0.500.tif
Ensemble_orbital_0.750.tif	Ensemble_wave_power_0.750.tif
Ensemble_orbital_0.9.tif	Ensemble_wave_power_0.9.tif
Ensemble_orbital_0.950.tif	Ensemble_wave_power_0.950.tif
Ensemble_orbital_0.995.tif	Ensemble_wave_power_0.995.tif
Ensemble_orbital_max.tif	Ensemble_wave_power_max.tif
Ensemble_orbital_mean.tif	Ensemble_wave_power_mean.tif

Ensemble_AllTimePoints
These are only available for wave heights and wave power since all other variables were set to "Not a Number" (NaN) for wave heights < 0.15 m to avoid spurious results.

Ensemble_Hs_0.250.tif
Ensemble_Hs_0.500.tif
Ensemble_Hs_0.750.tif
Ensemble_Hs_0.9.tif
Ensemble_Hs_0.950.tif
Ensemble_Hs_0.995.tif
Ensemble_Hs_max.tif
Ensemble_Hs_mean.tif
Ensemble_wave_power_0.250.tif
Ensemble_wave_power_0.500.tif
Ensemble_wave_power_0.750.tif
Ensemble_wave_power_0.9.tif
Ensemble_wave_power_0.950.tif
Ensemble_wave_power_0.995.tif
Ensemble_wave_power_max.tif
Ensemble_wave_power_mean.tif

Wave time series (Tier2B DWDB)
Hindcast and projected time series for two different locations.

CMIP6_tseries_LatLon_70.27_-147.59.mat
CMIP6_tseries_LatLon_70.33_-147.36.mat
ERA5_tseries_LatLon_70.27_-147.59.mat
ERA5_tseries_LatLon_70.33_-147.36.mat

Appendix B: Supplementary figures

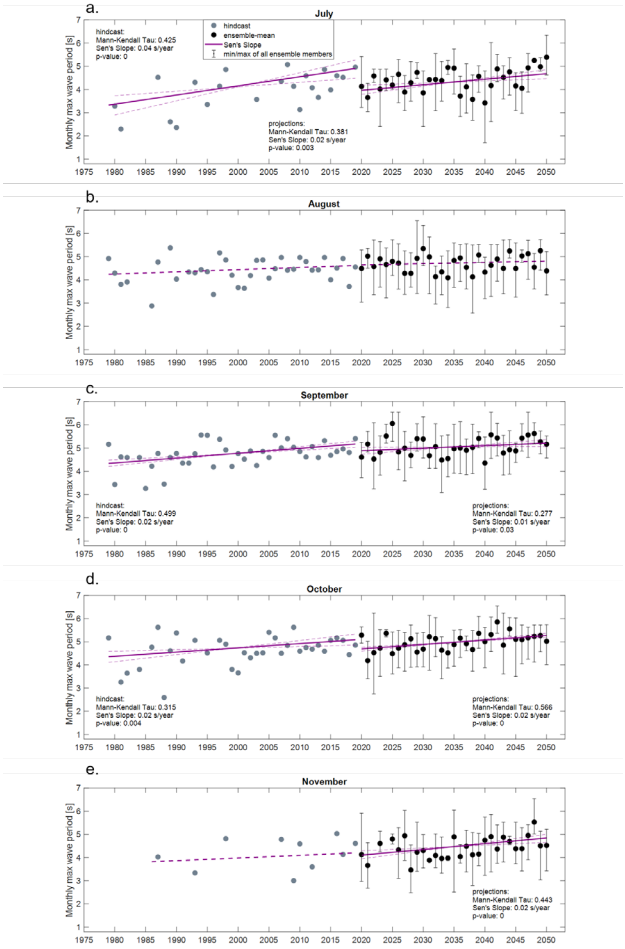

Figure B.1. Time-series plots of monthly annual maximum wave periods at N70.27458º / W147.5863º from 1979 through 2050.
Maxima are shown for the open water months July through November (a.-e.).

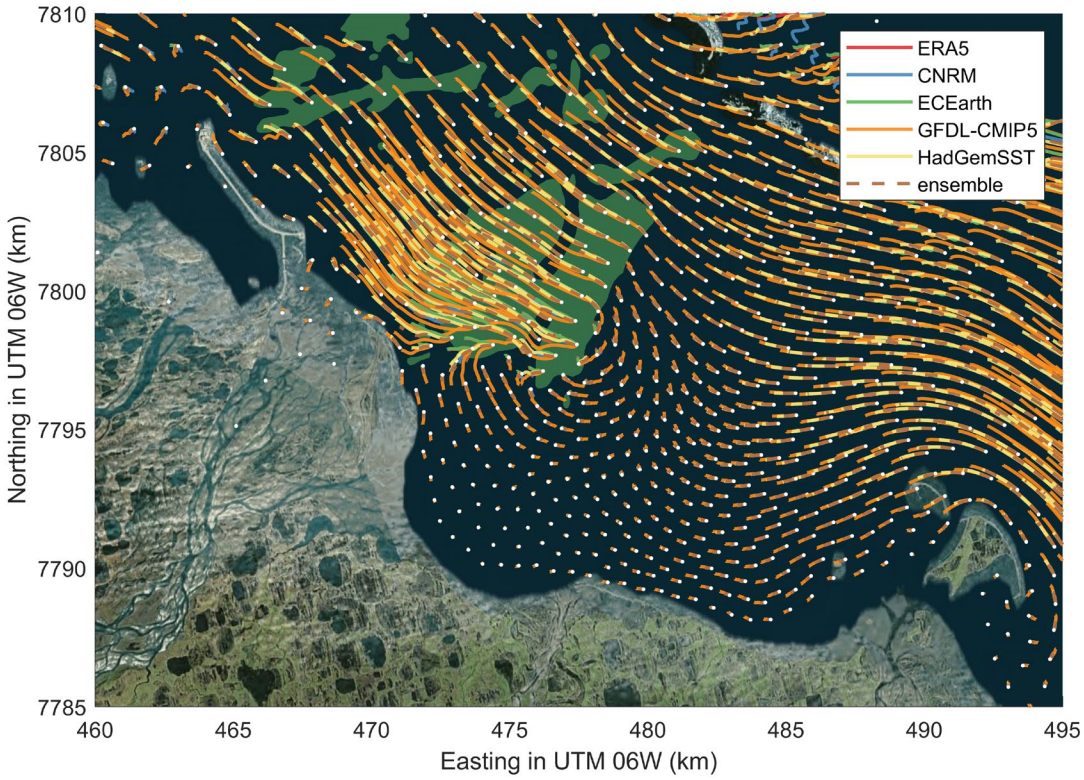

Figure B.2. Mapped comparisons of the mean sediment transport potentials as visualized with SedTRAILS for the hindcast using ERA5 forcing and projections from each GCM forced model run.

All simulations assume no LDI construction. Red and blue curved lines indicate directions of sediment transport potentials, with the points intended to illustrate an initial starting location of a virtual sediment particle. Panel (a.) shows the mean sediment transport

U.S. Department of the Interior (DOI)
DOI protects and manages the Nation's natural resources and cultural heritage; provides scientific and other information about those resources; and honors the Nation's trust responsibilities or special commitments to American Indians, Alaska Natives, and affiliated island communities.

Bureau of Ocean Energy Management (BOEM)
BOEM's mission is to manage development of U.S. Outer Continental Shelf energy and mineral resources in an environmentally and economically responsible way.

BOEM Environmental Studies Program
The mission of the Environmental Studies Program is to provide the information needed to predict, assess, and manage impacts from offshore energy and marine mineral exploration, development, and production activities on human, marine, and coastal environments. The proposal, selection, research, review, collaboration, production, and dissemination of each of BOEM's Environmental Studies follows the DOI Code of Scientific and Scholarly Conduct, in support of a culture of scientific and professional integrity, as set out in the DOI Departmental Manual (305 DM 3).